Geological Magazine

www.cambridge.org/geo

Original Article

Cite this article: Ahmadvand A, Ghorbani MR, Mokhtari MAA, Chen Y, Amidon W, Santos JF, and Paydari M (2021) Lithospheric mantle, asthenosphere, slab and crustal contribution to petrogenesis of Eocene to Miocene volcanic rocks from the west Alborz Magmatic Assemblage, SE Ahar, Iran. *Geological Magazine* **158**: 375–406. https://doi.org/10.1017/S0016756820000527

Received: 7 September 2019
Revised: 28 April 2020
Accepted: 7 May 2020
First published online: 10 July 2020

Keywords:
west Alborz Magmatic Assemblage; subalkali basalts–andesites; high-Nb basalts; A-type rocks; mantle

Author for correspondence:
Mohammad Reza Ghorbani,
Email: ghorbani@modares.ac.ir

CAMBRIDGE UNIVERSITY PRESS

Lithospheric mantle, asthenosphere, slab and crustal contribution to petrogenesis of Eocene to Miocene volcanic rocks from the west Alborz Magmatic Assemblage, SE Ahar, Iran

Ahmad Ahmadvand[1], Mohammad Reza Ghorbani[1], Mir Ali Asghar Mokhtari[2], Yi Chen[3], William Amidon[4], Jose Francisco Santos[5] and Mohammad Paydari[1]

[1]Department of Geology, Tarbiat Modares University, Tehran, Iran; [2]Department of Geology, Faculty of Sciences, University of Zanjan, Iran; [3]State Key Laboratory of Lithospheric Evolution, Institute of Geology and Geophysics, Chinese Academy of Sciences, P.O. Box 9825, Beijing 100029, China; [4]Geology Department, Middlebury College, Middlebury, VT, 05753, USA and [5]Department of Geosciences, Geobiotec Research Unit, University of Aveiro, 3810-193, Aveiro, Portugal

Abstract

Significant uncertainty remains regarding the exact timing and nature of subduction events during the closure of the Tethyan seas in what is now NW Iran. This study thus presents new geochemical compositions and U–Pb ages for a suite of volcanic rocks emplaced during Cenozoic volcanism in the west Alborz Magmatic Assemblage, which is commonly regarded as the back-arc of the Neotethyan magmatism in Central Iran. The subalkali basalts and andesites are dated to 57 ± 1.2 Ma, and are likely derived from a supra-subduction mantle wedge. Later, trachytic A-type rocks erupted from ~42 to 25 Ma during an anorogenic (extensional) stage triggered by slab retreat and associated asthenospheric mantle influx. A-type melts were at least partly concurrent with lithospheric mantle magmatism implied by eruption of subalkali basalts–andesites around 26–24 Ma. Next, Amp-Bt trachybasaltic volcanism with high-Nb basaltic affinity at ~19 Ma likely records slab deepening and slab partial melting, which reacted with the mantle wedge to produce the source material for the high-Nb basalts. Sr–Nd isotopic ratios for SE Ahar mafic as well as A-type rocks imply rather enriched mantle source(s). Some crustal contamination is implied by the presence of inherited zircons dominated by those derived from Neoproterozoic–Cambrian basement rocks and Carboniferous magmatism. Rhyolitic rocks with adakitic affinity probably mark the final volcanism in the study area. The adakitic rocks show crustal signatures such as high K and Th, probably formed as a consequence of higher temperature gradients, at crustal levels, imposed by both slab and mantle partial melts.

1. Introduction

Volcanic rocks from the west Alborz Magmatic Assemblage (AMA; Fig. 1) record the final closure of the Neotethys Sea, ultimately initiating continent–continent collision that formed the Alpine–Himalayan orogenic belt. However, numerous questions remain about the exact timing and geometry of subduction, specifically, when did trench roll-back and enhanced melting of metasomatically enriched mantle affect the region. Although the west AMA is an ideal site to study the evolution of the Tethyan margin, relatively few studies have addressed the geodynamic events that led to the evolution of magmatism along the margin. Except for a few prominent and mostly Quaternary volcanic edifices, the NW Iran Tertiary volcanic domains remain poorly understood. This study attempts to fill that gap by combining bulk-rock geochemistry and U–Pb zircon geochronology to reveal the sources and processes involved in generating the magmatic rocks of the SE Ahar region.

NW Iran (Fig. 1) sits at the intersection of four regional magmatic domains: the Urumieh–Dokhtar Magmatic Assemblage (UDMA), Central Iran, AMA and Lesser Caucasus domains, which surround the study area to the west, south, east and north, respectively (Aghanabati, 2004; Asiabanha & Foden, 2012; Jamali & Mehrabi, 2015; Moritz *et al.* 2016). The western part of the AMA is also known as the Alborz–Azerbaijan or Arasbaran (Nabavi, 1976; Babakhani *et al.* 1990; Allen *et al.* 2003; Mokhtari *et al.* 2010). The UDMA and AMA are two magmatic belts formed on the overlying Central Iranian Plate, underthrust by the Tethyan oceanic slab towards the northwest (Omrani *et al.* 2008). A chain of tectonic events stretching from the late Triassic Cimmerian orogeny to the Cenozoic collision of the Iranian Plate with Eurasia resulted in the development of the Alborz mountain range that includes the AMA (Jackson *et al.* 2002;

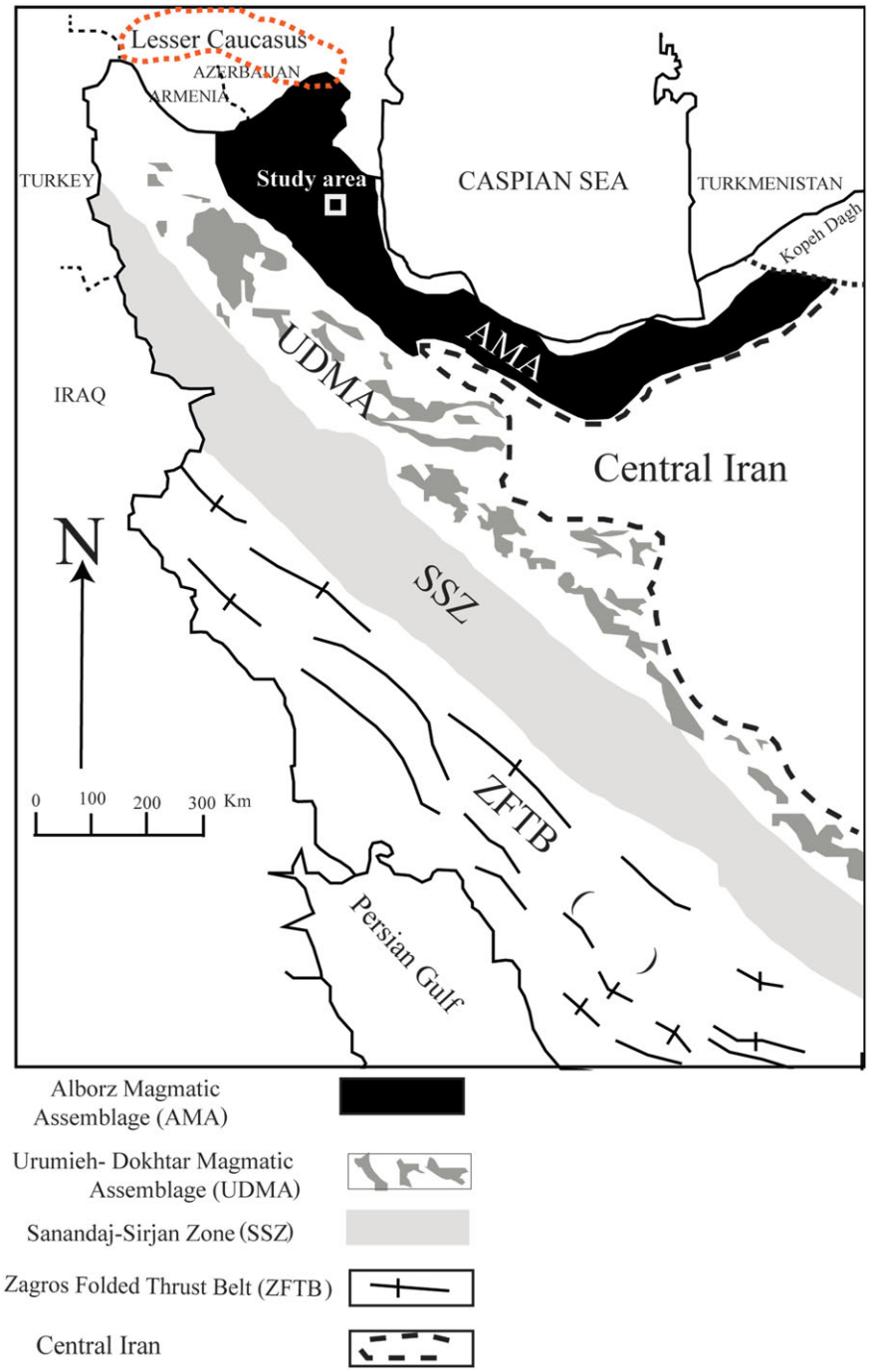

Fig. 1. (Colour online) Major tectonomagmatic units of Iran and the study area are shown on a map of Iran. The major structural units shown are after Alavi (1996). The present study area and adjacent regions might simply be referred to as the West Alborz Cenozoic magmatism or west AMA. The Lesser Caucasus domain is from Rolland (2017).

Hassanzadeh *et al.* 2008). The UDMA is considered to be the major magmatic arc, whereas the AMA is suggested to represent its extensional or back-arc setting (Asiabanha & Foden, 2012).

Previously published radiometric ages for magmatic rocks from the west AMA (online Supplementary Material Fig. S1) and UDMA (see fig. 1 in Babazadeh *et al.* 2017) are post-Eocene in age (e.g. Omrani *et al.* 2008; Nabatian *et al.* 2014). The similar age range and proximity of volcanic rocks in the UDMA and west AMA might suggest they were formed by the same processes. However, despite broad subduction-related compositional similarities between the UDMA and AMA volcanic rocks, there are significant geochemical differences. Specifically, volcanic rocks from the former are mainly calc-alkaline, whereas a large portion of volcanic rocks from the latter are alkaline and richer in trace elements (e.g. Jahangiri, 2007; Aghazadeh *et al.* 2010).

Although the above-mentioned studies have painted a basic picture of the sequence of events that formed the volcanic rocks of the west AMA, significant disagreement remains on the timing and nature of these events. Specifically, estimates of the age of Neotethyan oceanic closure range from Cretaceous (Berberian & King, 1981; Alavi, 1994) to Quaternary (Stöcklin, 1968). One model is that Paleocene slab break-off pre-dated flat-slab

https://doi.org/10.1017/S0016756820000527 Published online by Cambridge University Press

subduction (Agard *et al.* 2011, fig. 10 therein). Flat-slab subduction of the Neotethyan oceanic plate beneath Central Iran was then followed by an Eocene volcanic flare-up, including eruption of tholeiitic to calc-alkaline rocks (Verdel *et al.* 2011). Deepening of the slab continued through the Eocene period, ultimately prompting asthenospheric upwelling that developed a plume-derived signature in Oligocene time (Yeganehfar *et al.* 2013; Ghorbani *et al.* 2014). In a second and contrasting model, Omrani *et al.* (2008) argued that Arabia–Eurasia continental collision did not begin until Oligocene time. However, the most recent literature considers the Eocene–Oligocene (Allen & Armstrong, 2008; Horton *et al.* 2008; Dargahi *et al.* 2010) or Middle Miocene–Pliocene (Guest *et al.* 2006; Azizi & Moinevaziri, 2009) to be the most plausible ages for the onset of collision. This age range appears to have overlapped with the events that led to the back-arc development in the west AMA. A wide range of magmatic activity occurred in this period of time (e.g. Aghazadeh *et al.* 2011; Castro *et al.* 2013; Nabatian *et al.* 2014). Numerous works on collisional settings suggest that two or multiple source regions have been tapped to furnish partial melts for a variety of igneous rocks in a comparable period of time (e.g. Gao *et al.* 2010; Ersoy *et al.* 2017; Rezeau *et al.* 2017).

The main objective of the current study is thus to present new geochemical data and radiometric ages for the volcanic rocks of the west AMA to further elucidate the timing and nature of Tethyan subduction events. Importantly, this study presents new results for A-type and high-Nb Eocene to Late Miocene volcanic rocks and their geodynamic significance.

2. Geological overview

The AMA and the neighbouring UDMA are likely associated with early to late Cenozoic subduction-related magmatism on the Zagros hinterland (Berberian & King, 1981). The AMA, including the study area in SE Ahar, comprises basaltic–andesitic–dacitic lava and many granitoid intrusions with calc-alkaline to alkaline compositional affinity (M. Moayyed, unpub. Ph.D. thesis, Univ. Tabriz, 2001; Aghazadeh *et al.* 2011; Nabatian *et al.* 2014). These calc-alkaline and potassic rocks are interpreted as arc and back-arc magmatism in an extensional, post-collisional tectonic setting (Asiabanha & Foden, 2012; Castro *et al.* 2013; Nabatian *et al.* 2014).

Owing to its presumed back-arc affinity, the AMA is believed to have postdated the major magmatism of the UDMA. Based on interlayered fossiliferous beds, the major phase of subduction-related magmatic rocks from the UDMA was traditionally considered to have been Middle Eocene in age (Emami *et al.* 1996; Hajian, 2001). However, in recent years, dating of magmatic rocks from the UDMA and AMA revealed younger Oligocene and Miocene ages (Castro *et al.* 2013; Ghorbani *et al.* 2014). For example, Aghazadeh *et al.* (2010, 2011) dated intermediate plutonic rocks of the Arasbaran–Tarum batholith (part of the AMA) to ~28.9 Ma and 25 Ma. Given the prevailing view of older Eocene emplacement of the UDMA, they suggested that the back-arc volcanism recorded by the AMA is up to 30 Ma younger than magmatism along the main magmatic arc (the UDMA). However, subsequent work in the UDMA has revealed Oligocene and Miocene ages in the UDMA, suggesting that both domains experienced a complex history of magmatism, including significant post-Eocene magmatism (e.g. Chiu *et al.* 2013; Yeganehfar *et al.* 2013; Ghorbani *et al.* 2014; Babazadeh *et al.* 2017).

Cretaceous volcano-sedimentary sequences are the oldest rock units that crop out near to the study area; however, the presence of older crustal rocks is suggested by the inherited zircons retrieved from volcanic rocks in the present study. Palaeoproterozoic, Neoproterozoic–early Cambrian, Palaeozoic and Mesozoic ages (Hassanzadeh *et al.* 2008; Chaharlang & Ghorbani, 2020) obtained for inherited zircons from igneous rocks imply the presence of older crustal materials underlying the Alborz, Sanandaj–Sirjan and Central Iran tectonomagmatic zones. Igneous rocks in the study area entirely comprise Tertiary magmatic rocks, including Eocene, Oligocene and Miocene rock units (Figs 2, 3). The Eocene units include basaltic, andesitic to dacitic–rhyolitic lavas, dykes and shallow intrusive rocks. The Oligocene unit is basaltic, andesitic, trachyandesitic to trachytic, and the Miocene unit is mainly trachybasaltic in composition. They are intruded by large intermediate to felsic plutonic bodies. For example, the Youseflu plutonic body is composed of monzodiorite–monzonite and granite. Younger Oligocene units include the south Khankandi plutonic body, composed of granodiorite, quartz monzonite and monzonite to gabbro intruded at ~28.9 Ma (Aghazadeh *et al.* 2010). Finally, the Mizan plutonic bodies in the southern part of the study area include monzogabbro, monzonite, syenite and granites intruded at ~24 Ma (Castro *et al.* 2013).

The field relationships of the volcanic units in the study area are not conclusive. This is largely owing to the subsequent tectonomagmatic events. Specifically, significant portions of the study area have been affected by varying degrees of hydrothermal alteration imposed by multiple intrusive bodies (see above). However, original volcanic successions are maintained in some parts of the study area. The successions include mainly volcanic and pyroclastic rocks/beds demonstrating rather conformable contacts. The volcanic rocks are mainly basic to intermediate lava flows, whereas silica-richer bodies are felsic intrusive rocks/domes. Unfortunately, stratigraphic controls such as fossiliferous beds are absent in the study area.

3. Sampling and analytical methods

3.a. Sampling

The primary strategy for sampling was adopted based on the volcanic rock units portrayed on the Ahar geological map (1:100<2>000). Efforts were made to sample all volcanic lithologies, including some lithologies not depicted on the base geological map. A total of 220 hand specimens were collected; 115 of those were selected for thin-sectioning based on their freshness, lithological variety, geographic distribution and presumed timing in the volcanic succession.

3.b. Whole-rock major and trace elements

Whole-rock major- and trace-element concentrations were determined for 29 samples (Tables 1, 2) at the ALS Chemex Co. Ltd. in Guangzhou, China. Major-element oxides were measured on fused glass discs with lithium borate using a Phillips PW 1500 X-ray fluorescence (XRF) spectrometer. The analytical precision was better than 5 %, estimated from repeated analyses of the rock standards (GSR-1, GSR-4, GSR-9 and GSR-10; online Supplementary Material Table S1). Loss on ignition (LOI) was measured after heating to 1000 °C. Whole-rock trace elements were analysed using an Agilent 7700x inductively coupled plasma mass spectrometer (ICP-MS). The sample powder was added to lithium metaborate, mixed well and fused in a furnace at 1025 °C. After cooling, the samples were further digested in a distilled $HF + HNO_3$ solution in Teflon bombs for several days, evaporated to near dryness, then

https://doi.org/10.1017/S0016756820000527 Published online by Cambridge University Press

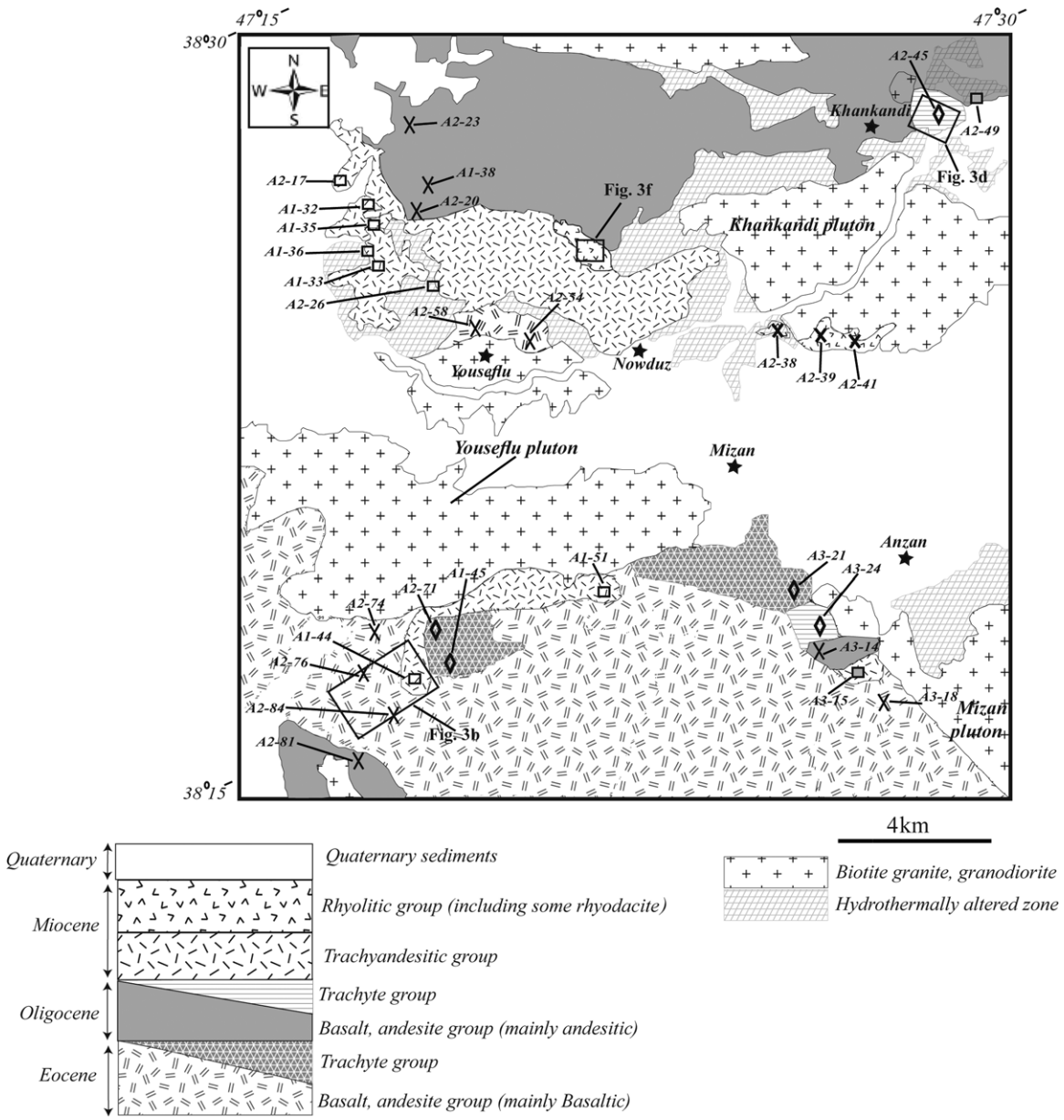

Fig. 2. Geological map of the study area in SE Ahar with major modifications after Mahdavi & Amini Fazl (1988). Rectangles indicated as Figures 3b, d and f refer to the areas portrayed/covered in the respective figures (see Fig. 3).

diluted using super-pure HNO_3 for ICP-MS analysis. The precision and accuracy for most trace elements were better than 5 % based on analyses of United States Geological Survey (USGS) rock standards (BCR-2, BHVO-2 and AGV-2; online Supplementary Material Table S2).

3.c. Sr and Nd isotopic analyses

Sr and Nd isotopic compositions were determined for ten samples (Tables 1, 3) at the Laboratorio de Geologia Isotopica da Universidade de Aveiro, Portugal. The selected powdered samples were dissolved in HF/HNO_3 solution in Teflon Parr acid digestion bombs at 180 °C for three days. After evaporation of the final solution, the samples were dissolved in HCl (6.2 N) and dried. The elements to be analysed were purified through the conventional ion chromatography technique in two stages: separation of Sr and rare earth elements (REEs) in an ion exchange column with AG8 50 W Bio-Rad cation exchange resin and purification of Nd from other lanthanide elements in columns with cation exchange Ln resin (Eichrom Technologies). All reagents used in the preparation of the samples were distilled through sub-boiling, and the water was produced by a Milli-Q Element (Millipore) apparatus. Sr was loaded on a single Ta filament with H_3PO_4, whereas Nd was loaded on a Ta outer-side filament with HCl in a triple filament arrangement. $^{87}Sr/^{86}Sr$ and $^{143}Nd/^{144}Nd$ isotopic ratios were determined through a multi-collector thermal ionization mass spectrometer (TIMS) VG Sector 54. Data were acquired in dynamic mode with peak measurements at 1–2 V for ^{88}Sr and 0.5–1.0 V for ^{144}Nd. Typical runs consisted of acquisition of 60 isotopic ratios. Sr and Nd isotopic ratios were corrected for mass fractionation relative to $^{88}Sr/^{86}Sr = 0.1194$ and $^{146}Nd/^{144}Nd = 0.7219$. During this study, the SRM-987

https://doi.org/10.1017/S0016756820000527 Published online by Cambridge University Press

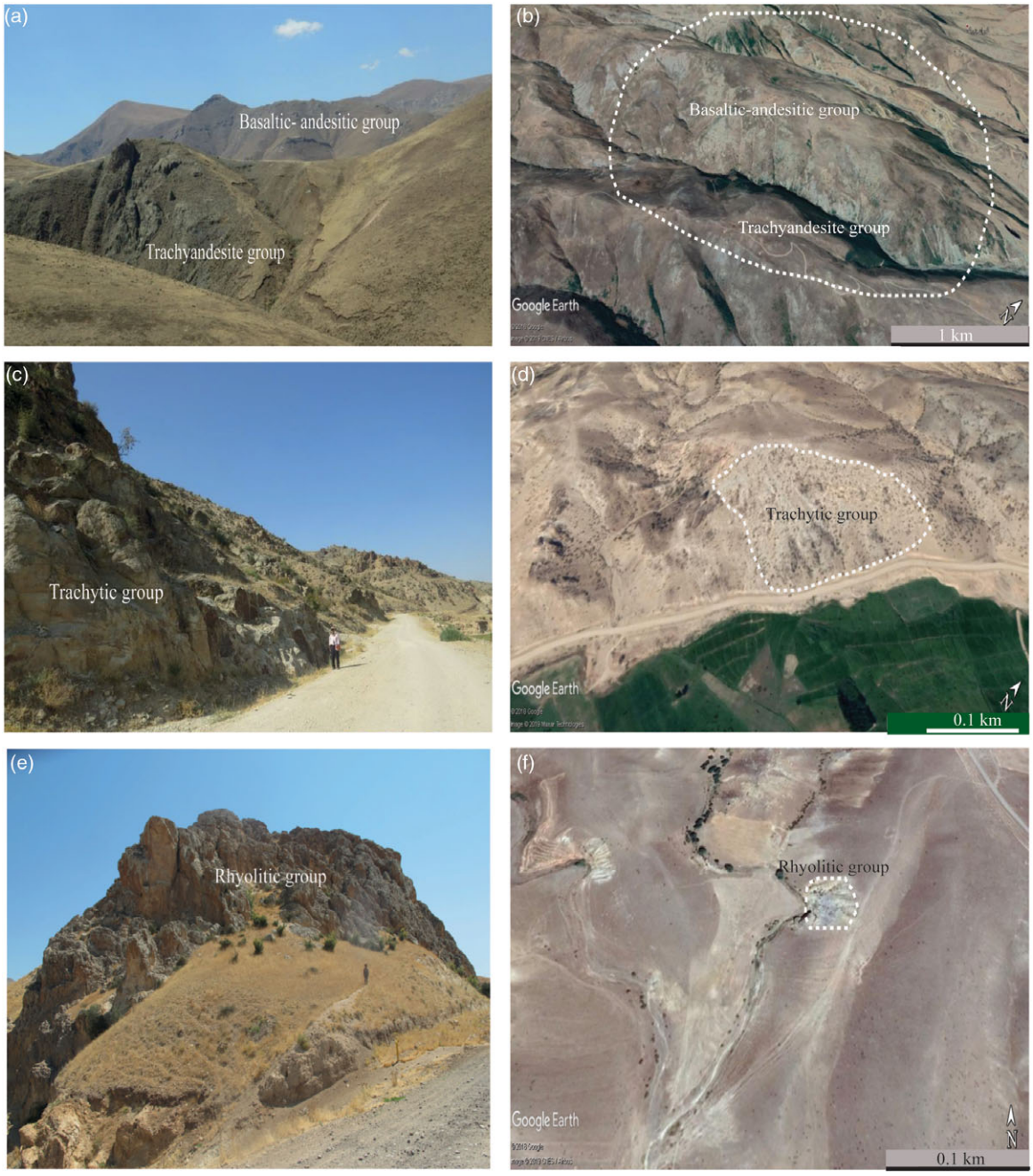

Fig. 3. (Colour online) (a, c, e) Field images of the volcanic rocks from SE Ahar and (b, d, f) their Google Earth counterparts. (a) Subalkali basalts–andesites and HNBs, 8 km south of Youseflu; (b) A-type (trachytic) rocks, near Khankandi; (c) adakitic (rhyolitic) rocks, 4 km NE of Youseflu. The scales for Google Earth images are shown at the lower right corner.

standard gave an average value of $^{87}Sr/^{86}Sr = 0.710266(14)$ (N = 13; confidence limit = 95 %), and the JNdi-1 standard gave an average value of $^{143}Nd/^{144}Nd = 0.5121016(59)$ (N = 10; confidence limit = 95 %).

3.d. U–Pb dating

The purified zircon separates were mounted in epoxy and polished to reveal cross-sections parallel to the c-axis. The abundances of ^{238}U, ^{235}U, ^{206}Pb and ^{207}Pb were measured (Tables 1, 4) using a NWR-213 laser coupled to a Thermo ICAP-Q quadrupole mass spectrometer at Middlebury College in Vermont, USA. A laser spot size of 20 µm was used along with a 40 µm spot used for two-second 'cleaning shots' prior to each ablation. We used a laser energy of 5.00 J/cm^2, a frequency of 10 Hz, dwell time of 30 seconds and a blank collection of 20 seconds. Isotopic fractionation was monitored and corrected using the primary zircon standard 91500 (Wiedenbeck *et al.* 1995), along with the secondary standards 94-35 and Plešovice analysed in blocks interspersed between sets of six unknowns. Data were reduced using the Iolite software (Paton *et al.* 2011), wherein any laser-shot time series showing multiple isotopic domains or strongly increasing or decreasing signals were discarded. Quoted uncertainties reflect the propagated uncertainties as exported from Iolite, which includes a propagated

https://doi.org/10.1017/S0016756820000527 Published online by Cambridge University Press

Table 1. Sample numbers and rock types used for geochemical data acquisition in the current study

Sample	Latitude	Longitude		Lithology	Geochemistry	U–Pb age dating	Sr–Nd isotopic ratios
A1-38	*38° 27′ 03″*	*47° 18′ 52″*	basaltic–andesitic group	Andesite	*		
A2-20	*38° 26′ 29″*	*47° 18′ 15″*		Andesite	*		
A2-23	*38° 28′ 15″*	*47° 18′ 00″*		Andesite	*	*	*
A2-58	*38° 24′ 34″*	*47° 20′ 42″*		Basaltic trachyandesite	*		
A2-74	*38° 18′ 45″*	*47° 18′ 08″*		Dacite	*		
A2-81	*38° 15′ 58″*	*47° 17′ 17″*		Andesite	*	*	*
A2-84	*38° 16′ 79″*	*47° 18′ 42″*		Andesite	*		*
A3-18	*38° 17′ 26″*	*47° 27′ 21″*		Basalt	*		*
A3-14	*38° 17′ 55″*	*47° 26′ 19″*		Basalt	*		
A2-54	*38° 24′ 30″*	*47° 21′ 10″*		Basaltic andesite	*	*	*
A2-76	*38° 17′ 16″*	*47° 17′ 53″*		Basaltic trachyandesite	*		
A3-15	*38° 17′ 46″*	*47° 26′ 59″*	High-K	Trachyandesite	*	*	*
A2-49	*38° 28′ 58″*	*47° 29′ 14″*	Low-K	Basaltic trachyandesite	*		
A2-38	*38° 24′ 41″*	*47° 25′ 55″*	Rhyolitic (adakitic group)	Trachydacite	*		
A2-39	*38° 24′ 24″*	*47° 26′ 47″*		Rhyolite	*		
A2-41	*38° 23′ 59″*	*47° 27′ 27″*		Rhyolite	*		
A1-45	*38° 17′ 58″*	*47° 19′ 02″*	Trachytic (A-type group)	Trachyte	*		
A2-45	*38° 28′ 40″*	*47° 28′ 16″*		Trachydacite	*	*	*
A3-21	*38° 18′ 50″*	*47° 25′ 29″*		Trachyte	*		
A3-24	*38° 18′ 17″*	*47° 26′ 29″*		Trachyte	*		
A2-71	*38° 18′ 16″*	*47° 19′ 06″*		Trachydacite	*	*	*
A1-32	*38° 26′ 59″*	*47° 17′ 35″*	High-Nb basaltic–andesitic group	Trachyandesite	*		
A1-33	*38° 25′ 10″*	*47° 17′ 46″*		Trachyandesite	*		
A1-35	*38° 26′ 20″*	*47° 17′ 40″*		Trachyandesite	*	*	*
A1-36	*38° 25′ 59″*	*47° 17′ 30″*		Basaltic trachyandesite	*		
A1-44	*38° 17′ 58″*	*47° 19′ 00″*		Trachyte	*		
A1-51	*38° 19′ 27″*	*47° 21′ 26″*		Basaltic trachyandesite	*		
A2-17	*38° 27′ 44″*	*47° 17′ 09″*		Trachyandesite	*		
A2-26	*38° 25′ 60″*	*47° 19′ 02″*		Trachyandesite	*		*

term for excess scatter in the secondary standards (e.g. step 5 in Horstwood *et al.* 2016). Quoted uncertainties do not include propagated uncertainties for long-term variance of the secondary standards, decay constant or common-Pb correction. Inverse Concordia diagrams (Fig. 4) were constructed using the Isoplot 4.1 add-in for Microsoft Excel (Ludwig, 1991). In addition to conventional U–Pb ages, a common-Pb corrected age is reported. Age estimates for each sample were estimated by taking the error weighted mean of the common-Pb corrected ages (labelled as '207corr' in Table 4). These ages were computed using the 'age7corr' function in Isoplot, which first computes an anchored least squares fit to the data in inverse-Concordia space and then computes the 207-corrected age by intersecting that line with the Concordia line.

4. Results

4.a. U–Pb geochronology

Seven samples were selected for zircon separation and age dating (Table 4). They were chosen to represent the whole spectrum of rock types identified in the study area based on mineralogy, texture and whole-rock geochemistry (see Section 4.c below). These include three subalkaline basalts–andesites (A2-54, A2-23 and A2-81) and four alkaline samples (two Amp-Bt trachybasalts, A1-35 and A3-15, and two trachytes, A2-71 and A2-45). For detailed mineralogy, texture and photomicrographs of these samples see online Supplementary Material Figure S2 and its caption. Rock samples yielded only 5 to 40 zircon grains each, limiting our ability to build stronger statistics on observed age populations.

https://doi.org/10.1017/S0016756820000527 Published online by Cambridge University Press

Table 2. Major oxide (wt %) and trace-element (ppm) contents of representative samples from SE Ahar volcanic rocks

Sample	A1-45	A2-45	A3-21	A3-24	A2-71	A1-32	A1-33	A1-35	A1-36	A1-44	A1-51	A2-17	A2-26
	Trachytic (A-type rocks)					High-Nb basalts (HNBs)							
Major elements (wt %)													
SiO_2	62.91	66.94	59.22	60.11	61.17	54.32	56.12	54.58	54.09	60.34	51.28	52.33	57.70
TiO_2	0.37	0.57	0.86	0.84	0.83	1.06	1.16	1.15	1.16	0.38	1.52	1.18	0.98
Al_2O_3	19.49	17.42	18.04	18.30	18.35	16.92	17.54	18.20	17.85	20.39	19.00	18.36	17.78
Fe_2O_3	3.01	2.48	5.22	5.35	5.48	6.73	7.21	7.52	7.86	2.57	10.42	7.28	6.17
MnO	0.08	0.01	0.06	0.06	0.06	0.10	0.08	0.09	0.13	0.08	0.15	0.29	0.12
MgO	0.45	0.13	0.59	0.42	0.60	2.11	1.70	2.44	2.64	0.31	1.72	1.11	2.04
CaO	0.42	0.24	1.34	1.23	1.12	6.14	5.13	5.24	6.25	3.21	6.02	6.87	4.74
Na_2O	5.62	5.24	3.05	4.01	4.79	4.03	4.03	4.26	4.49	6.20	4.14	4.04	4.72
K_2O	6.57	5.56	8.81	8.23	5.53	3.64	3.57	3.96	3.46	2.93	2.79	3.77	3.93
P_2O_5	0.14	0.20	0.41	0.37	0.43	0.48	0.58	0.63	0.63	0.07	0.73	0.62	0.51
LOI	1.01	1.23	1.72	0.55	1.37	3.54	3.25	1.46	1.57	3.53	1.73	3.78	0.92
Sum	100.07	100.02	99.32	99.47	99.73	99.07	100.37	99.53	100.13	100.01	99.50	99.63	99.61
Trace elements (ppm)													
Cr	20	10	40	80	30	200	110	20	30	<10	10	30	40
Ni	1.3	1.2	2.9	6.7	8.2	56.4	33.2	14.6	15.6	1.2	12.1	19.2	26.4
Ga	19.9	14.8	19.9	22.0	18.1	21.3	21.1	23.3	18.9	14.7	21.2	21.8	21.8
Cs	3.27	1.71	4.23	3.06	7.10	1.43	1.07	2.59	1.71	0.89	4.19	1.49	1.00
Rb	172.5	106.5	248.0	279.0	119.0	107.5	104.0	119.5	85.9	66.2	51.1	106.5	112.5
Ba	740	893	494	421	996	761	771	1060	821	870	1815	877	944
Th	32.9	31.3	18.65	20.6	14.15	23.5	21.8	24.4	22.2	26.2	19.05	21.7	25.9
U	5.12	7.93	2.24	2.56	2.37	5.10	3.21	7.29	6.08	6.87	4.46	6.13	7.57
Nb	41.7	52.0	31.3	31.8	23.4	37.5	44.4	37.1	29.3	35.7	40.0	34.4	43.5
Ta	2.8	3.5	1.9	2.0	1.3	2.8	2.8	2.2	2.1	2.1	2.3	2.2	2.5
La	60.9	79.8	52.6	54.0	41.1	56.3	62.6	76.4	62.5	86.7	75.1	60.1	63.5
Ce	163.0	144.0	99.5	102.5	85.5	105.0	115.0	146.0	118.5	141.0	142.0	110.5	118.5
Pb	23.4	4.3	31.5	35.1	21.6	15.4	15.0	20.2	20.6	21.0	11.3	17.3	16.8
Pr	11.7	14.3	10.7	11.5	8.6	11.0	12.0	15.4	13.3	12.4	14.9	12.3	12.1
Sr	323	261	291	208	411	846	887	1235	1055	1150	900	919	909
Nd	40.5	52.1	41.1	43.8	33.8	43.1	46.5	60.4	53.7	41.6	59.0	48.1	43.6
Zr	406	400	365	385	279	311	320	329	266	350	305	287	359
Hf	9.0	9.9	9.2	9.9	6.7	7.8	8.0	7.4	7.0	7.3	6.9	7.2	7.9
Sm	6.7	8.2	7.5	8.2	6.7	7.3	7.5	10.9	9.5	6.1	10.9	8.6	7.3
Eu	1.7	2.0	1.3	1.3	1.5	2.1	2.0	2.8	2.6	1.7	2.8	2.3	2.0
Ti	1900	2820	4730	4250	4370	5880	6600	6560	6480	2080	8200	6530	5600
Gd	5.0	5.3	6.3	6.6	5.4	5.4	5.1	7.7	7.6	4.1	8.5	6.6	5.3
Tb	0.7	0.7	0.9	1.0	0.7	0.7	0.7	1.0	0.9	0.6	1.1	0.8	0.7
Dy	4.6	3.9	5.7	6.3	4.6	3.9	3.8	5.0	4.9	3.3	6.3	4.5	3.8
Ho	0.9	0.7	1.1	1.3	0.9	0.7	0.7	0.9	0.9	0.6	1.1	0.8	0.7
Er	2.7	2.1	3.6	3.7	2.7	1.9	2.0	2.4	2.4	1.7	3.2	2.3	1.8
Tm	0.4	0.3	0.5	0.6	0.4	0.3	0.3	0.3	0.3	0.3	0.4	0.3	0.2

(*Continued*)

https://doi.org/10.1017/S0016756820000527 Published online by Cambridge University Press

Table 2. (*Continued*)

Sample	A1-45	A2-45	A3-21	A3-24	A2-71	A1-32	A1-33	A1-35	A1-36	A1-44	A1-51	A2-17	A2-26
	Trachytic (A-type rocks)					High-Nb basalts (HNBs)							
Yb	2.7	2.1	3.9	4.1	2.5	1.8	1.7	2.1	2.0	1.7	2.7	2.0	1.7
Y	25.0	20.8	36.9	34.7	28.8	22.8	20.9	28.1	25.9	17.5	33.6	26.1	24.0
Lu	0.5	0.3	0.6	0.7	0.4	0.3	0.3	0.3	0.3	0.3	0.4	0.3	0.2

Sample	A2-38	A2-39	A2-41	A1-38	A2-20	A2-23	A2-54	A2-58	A2-74	A2-76	A2-81	A2-84	A3-14	A3-18	A3-15	A2-49
	Rhyolitic (adakitic rocks)			Basaltic–andesitic rocks											High-K	Low-K
Major elements (wt %)																
SiO_2	64.22	67.98	74.30	59.06	57.12	58.20	53.22	54.84	64.06	52.21	60.68	60.49	49.25	49.49	53.15	52.01
TiO_2	0.48	0.38	0.17	0.65	0.88	0.88	1.02	0.90	0.50	1.16	0.60	0.51	1.14	0.91	0.81	1.20
Al_2O_3	16.04	15.23	14.12	17.08	17.72	17.40	18.20	18.57	17.08	17.91	17.52	17.06	16.88	13.74	19.24	17.73
Fe_2O_3	4.41	2.61	0.99	5.91	7.22	6.71	7.89	7.46	5.06	8.06	5.43	5.38	9.01	10.03	6.18	7.69
MnO	0.06	0.04	<0.01	0.10	0.10	0.10	0.16	0.10	0.04	0.13	0.11	0.08	0.14	0.15	0.10	0.16
MgO	1.64	0.83	0.10	2.06	3.05	2.67	3.42	3.38	0.44	5.01	0.94	2.12	7.35	10.20	2.41	3.52
CaO	1.36	2.31	0.29	5.57	7.29	6.29	8.99	6.66	2.19	7.77	4.99	5.04	9.63	11.00	5.50	6.46
Na_2O	4.70	4.17	3.44	3.89	3.78	3.83	3.65	4.94	2.85	4.12	3.94	3.70	3.39	2.14	3.32	5.87
K_2O	4.41	4.18	5.51	2.83	2.18	2.46	1.68	1.52	3.95	2.18	3.24	2.04	1.42	1.75	5.61	0.51
P_2O_5	0.29	0.23	0.03	0.36	0.33	0.31	0.36	0.39	0.22	0.61	0.24	0.20	0.49	0.37	0.65	0.64
LOI	1.72	1.50	0.75	1.87	0.61	1.04	1.03	1.34	3.38	0.73	2.29	2.71	0.71	0.19	2.37	3.76
Sum	99.33	99.46	99.70	99.38	100.28	99.89	99.62	100.10	99.77	99.89	99.98	99.33	99.41	99.97	99.34	99.55
Trace elements (ppm)																
Cr	30	30	10	30	40	20	40	60	40	120	30	80	350	710	50	30
Ni	17.6	12.5	1.8	12.0	12.8	9.8	12.8	15.6	7.4	42.2	5.0	5.2	84.6	250.0	17.6	23.6
Ga	16.9	14.1	14.6	15.5	19.9	20.2	19.4	19.1	18.4	20.0	16.5	15.3	17.8	13.7	16.5	17.2
Cs	1.39	1.70	1.47	0.92	0.97	1.16	0.41	0.43	5.60	2.90	9.28	2.54	1.01	1.02	1.39	0.32
Rb	120.5	92.4	156.5	53.6	45.8	55.7	30.8	23.6	133.0	48.7	85.0	52.6	29.5	30.8	121.5	15.0
Ba	839	645	421	721	778	786	575	730	944	747	833	584	482	576	921	112
Th	12.05	16.00	18.85	7.53	7.34	7.51	5.30	8.50	11.60	5.62	6.11	7.20	3.82	2.68	7.98	7.29
U	2.75	2.72	4.62	2.14	2.12	2.09	1.70	2.05	3.65	1.49	1.53	2.00	0.96	0.90	2.59	1.90
Nb	19.6	16.4	22.1	13.9	15.2	18.0	12.7	19.2	13.2	18.2	7.6	8.8	11.9	6.5	12.8	19.2
Ta	1.3	1.2	1.5	1.0	0.9	0.9	0.6	1.1	1.1	1.0	0.5	0.6	0.6	0.4	0.7	1.2
La	35.0	34.9	36.6	32.5	31.1	36.7	27.4	37.7	27.2	45.3	21.1	28.1	32.8	17.2	32.1	43.4
Ce	61.0	56.6	54.7	59.9	58.3	68.8	53.4	71.9	48.2	87.4	38.0	49.9	65.2	35.6	61.9	84.1
Pb	20.4	21.0	71.9	10.0	9.9	7.5	8.3	8.8	20.9	10.1	18.0	12.1	6.9	8.4	16.0	22.1
Pr	5.8	5.1	4.6	6.2	6.2	7.4	5.9	7.4	4.9	9.7	4.4	5.0	7.1	4.3	6.8	9.7
Sr	541	517	214	603	692	657	772	740	469	1100	591	437	842	654	649	637
Nd	20.7	17.2	14.8	24.4	24.3	28.9	24.4	29.4	18.9	39.7	17.9	19.1	29.3	18.8	27.2	39.4
Zr	170	140	134	146	161	181	123	176	158	167	124	115	110	75	161	162
Hf	3.9	3.7	3.5	4.1	4.0	4.2	3.2	4.6	4.0	4.5	3.5	3.1	2.8	2.0	4.0	4.3
Sm	3.2	2.5	2.1	4.2	4.8	5.3	4.8	5.3	3.5	6.8	3.3	3.2	5.5	4.0	5.1	7.1
Eu	0.9	0.7	0.5	1.3	1.4	1.6	1.5	1.6	1.0	2.2	0.9	1.0	1.6	1.3	1.4	2.0
Ti	2860	2150	1010	3690	5050	4960	5690	4830	2940	6420	3450	2950	6340	5300	4660	6450
Gd	2.1	1.7	1.3	3.6	4.1	4.4	4.3	4.4	3.0	5.3	2.7	2.6	4.5	3.6	4.2	5.6

(*Continued*)

https://doi.org/10.1017/S0016756820000527 Published online by Cambridge University Press

Table 2. (*Continued*)

Sample	A2-38	A2-39	A2-41	A1-38	A2-20	A2-23	A2-54	A2-58	A2-74	A2-76	A2-81	A2-84	A3-14	A3-18	A3-15	A2-49
	Rhyolitic (adakitic rocks)			Basaltic–andesitic rocks											High-K	Low-K
Tb	0.3	0.2	0.2	0.5	0.6	0.7	0.6	0.7	0.4	0.7	0.4	0.4	0.6	0.5	0.6	0.7
Dy	1.4	1.2	0.9	3.2	3.7	3.9	3.9	4.0	2.5	4.0	2.3	2.3	3.3	2.8	3.4	4.1
Ho	0.2	0.2	0.2	0.6	0.7	0.8	0.8	0.8	0.5	0.7	0.4	0.5	0.6	0.5	0.7	0.7
Er	0.7	0.6	0.5	1.9	2.3	2.3	2.1	2.3	1.5	1.8	1.3	1.3	1.6	1.4	2.0	2.0
Tm	0.1	0.1	0.1	0.3	0.3	0.3	0.3	0.3	0.2	0.2	0.2	0.2	0.2	0.2	0.3	0.3
Yb	0.7	0.6	0.7	1.8	2.2	2.1	1.9	2.3	1.5	1.6	1.3	1.3	1.4	1.3	1.9	1.8
Y	11.9	6.6	8.0	19.5	25.8	26.7	21.5	22.6	14.9	20.9	12.8	14.9	23	14.4	22.9	18.3
Lu	0.1	0.1	0.1	0.3	0.3	0.3	0.3	0.3	0.3	0.2	0.2	0.2	0.2	0.2	0.3	0.3

Table 3. Sr–Nd isotopic analyses of representative rocks from SE Ahar volcanic rocks

Sample	Rb (ppm)	Sr (ppm)	$^{87}Rb/^{86}Sr$	Error (2σ)	$^{87}Sr/^{86}Sr$	Error (2σ)	Initial $^{87}Sr/^{86}Sr$	Sm (ppm)	Nd (ppm)	$^{147}Sm/^{144}Nd$	Error (2σ)	$^{143}Nd/^{144}Nd$	Error (2σ)	Initial $^{143}Nd/^{144}Nd$	Initial ϵ_{Nd}	Age (Ma)
A2-45	107	261	1.186	0.034	0.705181	21	0.704767	8.23	52.1	0.096	0.005	0.512759	19	0.512743	2.7	25
A2-71	119	411	0.838	0.024	0.705115	18	0.704623	6.71	33.8	0.120	0.006	0.512693	18	0.512660	1.5	42
A1-35	120	1235	0.281	0.008	0.704801	24	0.704727	10.9	60.4	0.109	0.003	0.512804	21	0.512790	3.4	19
A2-26	113	909	0.360	0.010	0.704681	14	0.704585	7.34	43.6	0.102	0.005	0.512743	12	0.512731	2.3	19
A3-18	30.8	654	0.136	0.004	0.704910	24	0.704859	3.98	18.8	0.128	0.007	0.512688	16	0.512666	1.0	26
A2-54	30.8	772	0.115	0.003	0.704413	28	0.704320	4.81	24.4	0.119	0.006	0.512793	16	0.512749	3.0	57
A2-23	55.7	657	0.245	0.007	0.704516	24	0.704432	5.26	28.9	0.110	0.006	0.512793	14	0.512776	3.0	24
A2-84	52.6	437	0.348	0.010	0.705270	23	0.705141	3.19	19.1	0.101	0.005	0.512638	19	0.512621	0.0	26
A2-81	85.0	591	0.416	0.012	0.705066	24	0.704912	3.27	17.9	0.111	0.006	0.512656	18	0.512637	0.3	26
A3-15	122	649	0.544	0.015	0.705043	28	0.704906	5.09	27.2	0.113	0.006	0.512675	19	0.512661	0.9	18

Grains themselves were also tiny, ranging from 50 to 120 μm in length and 20 to 50 μm in width, ranging in morphology from slightly rounded to euhedral to fragments. To this end, only cores were analysed in an attempt to obtain high-quality ablations of single age domains. In this case, 'cores' is used to describe the physical centre of the grain, and does not imply the existence of a younger rim. Recognizing the young age of the zircons, ^{232}Th and ^{208}Pb were not measured in an effort to increase counting statistics on ^{207}Pb. Cathodoluminescence images were not obtained because of the small grain size and the lack of funding available for imaging.

The majority of zircon ages for the volcanic rocks from the study area represent crystallization ages (i.e. eruption age for volcanic rocks) of the host rocks. However, some older zircons are also present, which are regarded as inherited zircons.

4.a.1. Magmatic zircon ages

Estimates of eruptive age were made using the youngest cluster of '207-corrected' ages that were within uncertainty of each other. These seven samples present the following ages in chronological order: A2-54 (57.0 ± 1.2 Ma; n = 2), A2-71 (41.7 ± 1.2 Ma; n = 2), A2-81 (26.1 ± 0.4 Ma, n = 7), A2-45 (24.6 ± 0.6 Ma; n = 18), A2-23 (23.7 ± 1.0 Ma; n = 5), A1-35 (19.2 ± 0.3 Ma; n = 4) and A3-15 (18 Ma; n = 1). The errors provided are 2-sigma analytical uncertainties. However, these underestimate the true uncertainty on the eruptive age because they do not account for the possibility that younger grains were missed owing to the small number of analyses.

The stated ages should be viewed as maximum constraints on the eruptive age, given that (1) zircons can crystallize in a magma prior to eruption, (2) the youngest population of zircons may have been missed, and (3) it is possible that older zircons could have been mobilized into the melt by the melting of older magmatic rocks. Thus, age estimates based on larger numbers of grains are relatively robust, whereas estimates based on few grains should be treated with appropriate care.

4.a.2. Inherited zircon ages

These zircons can be classified into two groups: (1) inherited zircons captured from broadly coeval magmatic rocks, and (2) inherited zircons from potential basement crustal rocks that span Palaeoproterozoic to Cretaceous time (online Supplementary Material Fig. S3). Inherited zircons from coeval but older magmatic rocks in the Tertiary succession are only present in sample A2-81, an andesite; these include five grains yielding 52, 44, 43, 42 and 41 Ma ages. Inherited zircons from older crustal rocks are present

https://doi.org/10.1017/S0016756820000527 Published online by Cambridge University Press

Table 4. U–Pb data for zircons from SE Ahar volcanic rocks

	Measured ratios												Measured ages (Ma)			
A2-45	$^{207}Pb/^{235}U$	2s	$^{206}Pb/^{238}U$	2s	Err. corr.	$^{206}Pb/^{238}U$	2s	$^{207}Pb/^{206}Pb$	2s	Err. corr.	$^{207}Pb–^{235}U$	2s	$^{206}Pb–^{238}U$	2s	207cor	2s
1_8	0.0427	0.0053	0.0065	0.0003	0.66	154.3	6.0	0.048	0.005	−0.14	74.5	12.0	29.2	1.4	41.6	1.6
1_9	0.0448	0.0056	0.0062	0.0002	0.53	161.6	6.3	0.052	0.006	−0.21	59.5	9.5	25.9	1.0	39.5	1.6
1_6	0.0388	0.0048	0.0056	0.0003	0.75	178.9	8.3	0.051	0.006	0.03	66.0	14.0	28.8	1.4	35.7	1.7
1_16	**0.0372**	**0.0063**	**0.0045**	**0.0003**	**0.64**	**220.3**	**15.0**	**0.055**	**0.007**	**−0.30**	**45.4**	**9.3**	**25.0**	**1.1**	**28.9**	**2.0**
1_57	**0.0275**	**0.0037**	**0.0043**	**0.0002**	**0.17**	**231.5**	**10.7**	**0.046**	**0.006**	**0.14**	**43.0**	**6.6**	**26.3**	**1.0**	**27.8**	**1.3**
1_67	**0.0343**	**0.0049**	**0.0043**	**0.0002**	**0.32**	**232.0**	**11.3**	**0.056**	**0.007**	**0.20**	**41.3**	**4.9**	**26.9**	**1.1**	**27.4**	**1.4**
1_49	**0.0254**	**0.0032**	**0.0042**	**0.0002**	**0.14**	**237.7**	**9.6**	**0.044**	**0.005**	**0.25**	**36.2**	**4.7**	**24.9**	**1.1**	**27.1**	**1.1**
1_11	**0.0340**	**0.0044**	**0.0043**	**0.0002**	**0.07**	**234.7**	**10.5**	**0.060**	**0.007**	**0.29**	**36.4**	**4.8**	**24.9**	**1.0**	**26.9**	**1.2**
1_64	**0.0680**	**0.0150**	**0.0045**	**0.0002**	**0.76**	**223.2**	**11.0**	**0.100**	**0.017**	**−0.63**	**49.0**	**6.5**	**27.9**	**1.3**	**26.9**	**1.5**
1_46	**0.0272**	**0.0038**	**0.0042**	**0.0002**	**0.32**	**239.9**	**9.8**	**0.048**	**0.006**	**−0.12**	**32.2**	**4.1**	**23.9**	**1.1**	**26.8**	**1.1**
1_65	**0.0495**	**0.0068**	**0.0043**	**0.0002**	**0.70**	**230.4**	**10.6**	**0.082**	**0.010**	**−0.43**	**46.0**	**12.0**	**27.4**	**1.3**	**26.7**	**1.3**
1_58	**0.0770**	**0.0130**	**0.0045**	**0.0002**	**0.64**	**220.3**	**10.2**	**0.119**	**0.018**	**−0.47**	**49.0**	**12.0**	**26.7**	**1.4**	**26.5**	**1.4**
1_54	**0.0480**	**0.0130**	**0.0043**	**0.0002**	**0.78**	**234.7**	**11.6**	**0.077**	**0.017**	**−0.69**	**37.2**	**5.1**	**25.5**	**1.0**	**26.3**	**1.4**
1_52	**0.0281**	**0.0034**	**0.0041**	**0.0002**	**0.36**	**245.9**	**9.1**	**0.050**	**0.006**	**0.09**	**34.0**	**4.3**	**27.4**	**1.2**	**26.1**	**1.0**
1_60	**0.0416**	**0.0051**	**0.0042**	**0.0002**	**0.35**	**239.2**	**10.3**	**0.073**	**0.008**	**0.21**	**36.5**	**4.9**	**25.7**	**1.1**	**26.0**	**1.2**
1_53	**0.0278**	**0.0039**	**0.0041**	**0.0002**	**0.05**	**246.9**	**10.4**	**0.050**	**0.007**	**0.16**	**34.2**	**4.8**	**27.7**	**1.3**	**25.9**	**1.1**
1_1	**0.0258**	**0.0036**	**0.0040**	**0.0002**	**0.06**	**249.3**	**9.3**	**0.047**	**0.006**	**0.03**	**27.5**	**3.6**	**27.8**	**1.3**	**25.8**	**1.0**
1_14	**0.0292**	**0.0047**	**0.0040**	**0.0002**	**0.03**	**247.5**	**11.0**	**0.052**	**0.008**	**0.12**	**42.5**	**5.1**	**41.6**	**1.6**	**25.8**	**1.2**
1_47	**0.0274**	**0.0035**	**0.0040**	**0.0002**	**0.27**	**248.8**	**9.9**	**0.050**	**0.006**	**0.14**	**38.7**	**4.7**	**36.0**	**1.7**	**25.8**	**1.0**
1_48	**0.0287**	**0.0038**	**0.0040**	**0.0002**	**0.28**	**249.4**	**11.2**	**0.050**	**0.006**	**0.28**	**25.5**	**3.1**	**27.1**	**1.1**	**25.7**	**1.2**
1_12	**0.0500**	**0.0130**	**0.0042**	**0.0002**	**0.83**	**241.0**	**12.8**	**0.079**	**0.014**	**−0.65**	**37.0**	**6.1**	**29.2**	**2.0**	**25.6**	**1.4**
1_66	**0.0295**	**0.0042**	**0.0040**	**0.0002**	**0.09**	**252.5**	**11.5**	**0.052**	**0.007**	**0.16**	**28.1**	**3.3**	**26.2**	**1.0**	**25.3**	**1.2**
1_7	**0.0434**	**0.0068**	**0.0041**	**0.0002**	**0.23**	**244.7**	**9.6**	**0.078**	**0.011**	**0.08**	**31.1**	**3.9**	**24.8**	**1.1**	**25.2**	**1.1**
1_5	**0.0277**	**0.0035**	**0.0039**	**0.0002**	**0.46**	**253.5**	**10.3**	**0.052**	**0.006**	**0.07**	**29.2**	**4.6**	**26.0**	**1.2**	**25.2**	**1.0**
1_56	**0.0282**	**0.0036**	**0.0039**	**0.0002**	**0.33**	**253.8**	**11.0**	**0.051**	**0.006**	**0.25**	**27.4**	**3.5**	**25.9**	**1.0**	**25.2**	**1.1**
1_10	**0.0291**	**0.0037**	**0.0039**	**0.0002**	**0.13**	**254.2**	**9.7**	**0.053**	**0.006**	**0.27**	**25.9**	**3.6**	**25.8**	**1.0**	**25.1**	**1.0**
1_3	**0.0367**	**0.0050**	**0.0040**	**0.0002**	**0.36**	**250.0**	**10.6**	**0.067**	**0.009**	**−0.01**	**27.2**	**3.8**	**26.8**	**1.1**	**25.1**	**1.1**
1_2	**0.0374**	**0.0052**	**0.0040**	**0.0002**	**0.46**	**252.8**	**10.2**	**0.070**	**0.009**	**−0.23**	**27.8**	**3.8**	**26.1**	**1.1**	**24.7**	**1.0**
1_62	**0.0311**	**0.0039**	**0.0039**	**0.0002**	**0.04**	**259.1**	**10.7**	**0.058**	**0.007**	**0.41**	**28.2**	**3.6**	**25.3**	**1.1**	**24.5**	**1.0**
1_15	**0.0276**	**0.0035**	**0.0038**	**0.0002**	**0.17**	**261.6**	**11.0**	**0.053**	**0.006**	**0.24**	**29.1**	**3.6**	**25.3**	**1.0**	**24.4**	**1.0**
1_55	**0.0363**	**0.0048**	**0.0039**	**0.0002**	**0.38**	**258.4**	**11.4**	**0.068**	**0.008**	**0.15**	**27.8**	**3.4**	**25.4**	**1.1**	**24.2**	**1.1**
1_63	**0.0365**	**0.0049**	**0.0039**	**0.0002**	**0.05**	**258.4**	**10.7**	**0.069**	**0.009**	**0.29**	**29.4**	**4.2**	**25.5**	**1.2**	**24.2**	**1.0**
1_61	**0.0461**	**0.0100**	**0.0039**	**0.0002**	**0.64**	**257.7**	**11.3**	**0.084**	**0.015**	**−0.45**	**28.8**	**3.7**	**25.8**	**1.2**	**23.8**	**1.1**

1_59	**0.0606**	**0.0099**	**0.0040**	**0.0002**	**0.06**	**248.7**	**9.9**	**0.111**	**0.017**	**0.09**	**44.4**	**5.4**	**39.8**	**1.5**	**23.7**	**1.1**
1_45	**0.0246**	**0.0031**	**0.0037**	**0.0002**	**0.04**	**273.1**	**11.9**	**0.049**	**0.006**	**0.42**	**24.9**	**3.0**	**23.6**	**1.0**	**23.5**	**1.0**
1_50	**0.0323**	**0.0041**	**0.0037**	**0.0002**	**0.12**	**269.5**	**12.4**	**0.063**	**0.008**	**0.48**	**27.6**	**3.4**	**24.6**	**1.0**	**23.4**	**1.1**
1_4	**0.0221**	**0.0026**	**0.0033**	**0.0001**	**0.45**	**300.7**	**11.8**	**0.048**	**0.005**	**0.35**	**22.2**	**2.6**	**21.4**	**0.8**	**21.4**	**0.8**
A2-71	$^{207}Pb/^{235}U$	2s	$^{206}Pb/^{238}U$	2s	Err. corr.	$^{206}Pb/^{238}U$	2s	$^{207}Pb/^{206}Pb$	2s	Err. corr.	$^{207}Pb–^{235}U$	2s	$^{206}Pb–^{238}U$	2s	207cor	2s
71_19	0.6710	0.0220	0.0813	0.0030	0.40	12.3	0.5	0.061	0.002	0.68	525.9	14.0	504.0	18.0	NA	NA
1_124	0.5930	0.0690	0.0719	0.0029	0.85	13.9	0.6	0.059	0.006	0.23	472.5	44.0	447.7	18.0	NA	NA
1_107	0.4860	0.0570	0.0628	0.0027	0.90	15.9	0.7	0.056	0.006	0.34	401.6	39.0	392.6	16.0	NA	NA
71_23	0.5870	0.0470	0.0568	0.0025	0.49	17.6	0.8	0.075	0.004	−0.23	463.0	28.0	356.0	15.0	NA	NA
71_12	0.4240	0.0160	0.0461	0.0019	0.68	21.7	0.9	0.067	0.002	0.58	358.6	11.0	290.8	12.0	NA	NA
1_103	0.2720	0.0420	0.0309	0.0031	0.98	32.4	3.2	0.064	0.007	−0.52	241.0	34.0	196.0	19.0	NA	NA
1_120	0.2070	0.0290	0.0210	0.0012	0.71	47.6	2.7	0.071	0.008	−0.18	190.0	25.0	133.8	7.8	NA	NA
71_3	0.0768	0.0054	0.0110	0.0005	0.30	90.7	3.8	0.050	0.003	0.26	75.0	5.1	70.7	3.0	70.5	2.9
1_109	0.0691	0.0120	0.0097	0.0004	0.12	103.0	4.7	0.051	0.008	−0.11	67.6	11.0	62.3	2.8	62.0	2.9
71_5	0.0659	0.0083	0.0091	0.0003	0.09	109.4	4.1	0.052	0.006	0.18	64.4	7.9	58.7	2.2	58.3	2.2
1_97	0.0711	0.0110	0.0090	0.0004	0.09	111.7	4.6	0.058	0.008	0.19	69.5	10.0	57.4	2.3	56.7	2.4
1_127	0.0534	0.0066	0.0082	0.0004	0.82	121.7	5.6	0.047	0.005	−0.08	52.8	6.3	52.7	2.4	52.8	2.5
71_6	0.0486	0.0030	0.0071	0.0002	0.10	141.4	4.8	0.050	0.003	0.31	48.2	2.9	45.4	1.6	45.2	1.5
1_100	**0.0454**	**0.0059**	**0.0065**	**0.0003**	**−0.09**	**153.1**	**5.9**	**0.051**	**0.006**	**0.23**	**45.1**	**5.7**	**42.0**	**1.6**	**41.8**	**1.6**
1_116	**0.0439**	**0.0054**	**0.0065**	**0.0003**	**0.20**	**153.8**	**6.2**	**0.050**	**0.006**	**0.24**	**43.6**	**5.2**	**41.8**	**1.6**	**41.6**	**1.7**
A1-35	$^{207}Pb/^{235}U$	2s	$^{206}Pb/^{238}U$	2s	Err. corr.	$^{206}Pb/^{238}U$	2s	$^{207}Pb/^{206}Pb$	2s	Err. corr.	$^{207}Pb–^{235}U$	2s	$^{206}Pb–^{238}U$	2s	207cor	2s
35_4	11.1500	0.3500	0.4480	0.0150	0.81	2.2	0.1	0.177	0.004	0.69	2534.0	29.0	2385.0	68.0	NA	NA
35_22	1.1000	0.0350	0.1183	0.0036	0.72	8.5	0.3	0.067	0.002	0.32	752.6	17.0	721.0	21.0	NA	NA
35_17	0.6076	0.0190	0.0771	0.0025	0.60	13.0	0.4	0.057	0.001	0.62	481.8	12.0	479.9	16.0	NA	NA
35_18	0.3830	0.0280	0.0449	0.0015	0.41	22.3	0.7	0.063	0.004	−0.10	331.0	21.0	283.0	9.2	NA	NA
35_24	0.0555	0.0023	0.0084	0.0003	0.75	119.8	4.4	0.049	0.002	−0.02	54.8	2.2	53.6	2.0	53.5	2.0
35_23	0.0516	0.0026	0.0075	0.0003	0.21	133.2	5.3	0.050	0.003	0.38	51.0	2.5	48.2	1.9	48.1	1.9
35_20	**0.0194**	**0.0008**	**0.0030**	**0.0001**	**0.39**	**333.1**	**12.2**	**0.047**	**0.002**	**0.40**	**19.5**	**0.8**	**19.3**	**0.7**	**19.3**	**0.7**
35_16	**0.0214**	**0.0010**	**0.0030**	**0.0001**	**0.37**	**332.1**	**12.1**	**0.052**	**0.002**	**0.16**	**21.5**	**1.0**	**19.4**	**0.7**	**19.3**	**0.7**
35_10	**0.0194**	**0.0008**	**0.0030**	**0.0001**	**0.25**	**334.2**	**10.8**	**0.047**	**0.002**	**0.30**	**19.5**	**0.8**	**19.3**	**0.6**	**19.2**	**0.6**
35_19	**0.0204**	**0.0010**	**0.0030**	**0.0001**	**0.15**	**338.3**	**11.4**	**0.050**	**0.002**	**0.37**	**20.5**	**1.0**	**19.0**	**0.7**	**18.9**	**0.6**
35_14	**0.0264**	**0.0023**	**0.0028**	**0.0001**	**0.59**	**358.7**	**12.9**	**0.069**	**0.005**	**−0.31**	**26.4**	**2.3**	**18.0**	**0.7**	**17.4**	**0.6**
A2-81	$^{207}Pb/^{235}U$	2s	$^{206}Pb/^{238}U$	2s	Err. corr.	$^{206}Pb/^{238}U$	2s	$^{207}Pb/^{206}Pb$	2s	Err. corr.	$^{207}Pb–^{235}U$	2s	$^{206}Pb–^{238}U$	2s	207cor	2s
81_9	0.0617	0.0073	0.0069	0.0002	0.04	145.3	5.1	0.065	0.008	0.07	60.5	6.9	44.2	1.6	43.2	1.6
81_28	0.0494	0.0041	0.0067	0.0002	0.00	148.6	5.3	0.053	0.004	0.25	48.9	4.0	43.2	1.5	42.9	1.5

(*Continued*)

Table 4. (*Continued*)

A2-81	$^{207}Pb/^{235}U$	2s	$^{206}Pb/^{238}U$	2s	Err. corr.	$^{206}Pb/^{238}U$	2s	$^{207}Pb/^{206}Pb$	2s	Err. corr.	$^{207}Pb–^{235}U$	2s	$^{206}Pb–^{238}U$	2s	207cor	2s
81_20	0.2185	0.0110	0.0082	0.0003	0.17	122.2	4.3	0.192	0.009	0.30	200.3	9.1	52.5	1.9	42.8	1.7
1_34	0.0522	0.0066	0.0067	0.0003	0.27	149.3	6.5	0.056	0.007	0.38	51.6	6.4	43.0	1.8	42.5	1.9
1_23	0.0619	0.0120	0.0066	0.0003	0.00	150.8	6.4	0.067	0.013	0.20	60.5	11.0	42.6	1.8	41.5	1.9
1_22	0.0471	0.0075	0.0065	0.0003	0.16	154.1	6.4	0.052	0.008	0.02	46.6	7.3	41.7	1.8	41.4	1.8
1_41	0.0433	0.0062	0.0064	0.0003	0.00	155.5	6.3	0.048	0.007	0.28	43.5	5.9	41.3	1.7	41.2	1.7
81_7	0.0576	0.0061	0.0065	0.0003	0.06	153.6	6.4	0.065	0.007	0.17	56.6	5.8	41.8	1.7	40.9	1.7
1_29	0.0880	0.0160	0.0065	0.0003	0.00	152.9	6.5	0.097	0.018	0.12	85.0	15.0	42.0	1.8	39.3	1.9
1_40	**0.0610**	**0.0140**	**0.0045**	**0.0003**	**0.53**	**223.7**	**14.5**	**0.098**	**0.019**	**−0.33**	**60.0**	**13.0**	**28.8**	**1.9**	**26.9**	**1.9**
1_30	**0.1300**	**0.0290**	**0.0050**	**0.0004**	**0.00**	**200.0**	**15.2**	**0.178**	**0.036**	**0.27**	**121.0**	**25.0**	**32.2**	**2.4**	**26.8**	**2.5**
1_28	**0.0359**	**0.0049**	**0.0042**	**0.0002**	**0.12**	**238.2**	**9.6**	**0.062**	**0.009**	**0.00**	**35.7**	**4.7**	**27.0**	**1.1**	**26.5**	**1.1**
81_14	**0.0378**	**0.0062**	**0.0042**	**0.0002**	**0.72**	**239.2**	**9.2**	**0.060**	**0.007**	**−0.55**	**36.0**	**5.2**	**26.9**	**1.0**	**26.4**	**1.0**
81_17	**0.0960**	**0.0230**	**0.0046**	**0.0003**	**0.15**	**219.3**	**12.5**	**0.141**	**0.027**	**−0.14**	**91.0**	**20.0**	**29.3**	**1.6**	**25.8**	**1.8**
81_6	**0.0402**	**0.0057**	**0.0041**	**0.0001**	**0.34**	**242.8**	**7.7**	**0.071**	**0.010**	**−0.20**	**39.8**	**5.5**	**26.5**	**0.9**	**25.7**	**0.9**
1_19	**0.0503**	**0.0080**	**0.0042**	**0.0002**	**0.32**	**238.2**	**9.6**	**0.086**	**0.013**	**−0.13**	**49.7**	**7.7**	**27.0**	**1.1**	**25.6**	**1.1**
A2-23	$^{207}Pb/^{235}U$	2s	$^{206}Pb/^{238}U$	2s	Err. corr.	$^{206}Pb/^{238}U$	2s	$^{207}Pb/^{206}Pb$	2s	Err. corr.	$^{207}Pb–^{235}U$	2s	$^{206}Pb–^{238}U$	2s	207cor	2s
1_73	8.5800	1.0000	0.3718	0.0150	0.69	2.7	0.1	0.167	0.018	0.43	2296.0	100.0	2037.0	71.0	NA	NA
1_74	5.7400	0.6600	0.3436	0.0140	0.88	2.9	0.1	0.121	0.013	0.46	1936.0	100.0	1908.0	67.0	NA	NA
23_5	1.7020	0.1000	0.1475	0.0048	0.53	6.8	0.2	0.082	0.004	−0.35	995.0	31.0	887.0	27.0	NA	NA
23_17	1.1950	0.0390	0.1338	0.0042	0.57	7.5	0.2	0.065	0.002	0.32	798.0	18.0	809.0	24.0	NA	NA
1_93	1.3030	0.1500	0.1332	0.0053	0.55	7.5	0.3	0.071	0.008	0.31	846.0	68.0	806.0	30.0	NA	NA
1_88	1.2240	0.1500	0.1260	0.0061	0.50	7.9	0.4	0.071	0.008	0.33	821.0	76.0	764.0	35.0	NA	NA
1_85	1.0770	0.1300	0.1213	0.0046	0.64	8.2	0.3	0.064	0.007	0.31	741.0	62.0	738.0	26.0	NA	NA
23_15	0.8960	0.0270	0.1096	0.0033	0.56	9.1	0.3	0.060	0.001	0.55	649.2	14.0	670.5	19.0	NA	NA
1_81	0.8730	0.1000	0.1092	0.0044	0.52	9.2	0.4	0.059	0.006	0.53	637.0	56.0	668.0	26.0	NA	NA
23_11	0.8860	0.1100	0.1092	0.0072	0.85	9.2	0.6	0.059	0.006	0.30	682.0	18.0	667.0	23.0	NA	NA
1_89	0.9600	0.0350	0.1091	0.0039	0.74	9.2	0.3	0.063	0.002	0.38	644.0	61.0	667.0	42.0	NA	NA
1_86	0.7920	0.0930	0.0991	0.0039	0.66	10.1	0.4	0.060	0.006	0.40	592.0	53.0	609.0	23.0	NA	NA
1_68	0.8290	0.0970	0.0985	0.0036	0.25	10.2	0.4	0.061	0.007	−0.11	612.0	54.0	605.8	21.0	NA	NA
23_13	0.7940	0.0260	0.0982	0.0033	0.93	10.2	0.3	0.059	0.001	0.69	592.9	15.0	603.0	19.0	NA	NA
23_16	0.8560	0.0280	0.0938	0.0031	0.58	10.7	0.4	0.067	0.002	0.48	627.4	15.0	578.0	18.0	NA	NA
23_12	0.7080	0.0230	0.0889	0.0029	0.78	11.2	0.4	0.057	0.001	0.54	543.1	13.0	548.9	17.0	NA	NA
1_70	0.6990	0.0810	0.0855	0.0033	0.72	11.7	0.5	0.059	0.006	0.39	538.0	49.0	529.0	19.0	NA	NA
1_82	0.4730	0.0560	0.0611	0.0023	0.68	16.4	0.6	0.055	0.006	0.20	392.7	38.0	382.6	14.0	NA	NA

23_18	0.3718	0.0140	0.0535	0.0017	0.65	18.7	0.6	0.051	0.001	−0.04	320.7	10.0	336.2	11.0	NA	NA
1_91	0.3090	0.0380	0.0413	0.0023	0.89	24.2	1.3	0.055	0.006	0.09	277.0	30.0	263.0	14.0	NA	NA
1_71	**0.0630**	**0.0140**	**0.0043**	**0.0002**	**0.63**	**231.5**	**11.3**	**0.108**	**0.021**	**−0.48**	**62.0**	**13.0**	**27.8**	**1.4**	**25.6**	**1.5**
1_72	**0.0294**	**0.0040**	**0.0040**	**0.0002**	**0.13**	**251.6**	**10.1**	**0.053**	**0.007**	**0.30**	**29.4**	**3.9**	**25.6**	**1.0**	**25.4**	**1.0**
23_1	**0.0281**	**0.0021**	**0.0039**	**0.0001**	**−0.06**	**254.1**	**8.4**	**0.051**	**0.004**	**0.27**	**28.1**	**2.1**	**25.3**	**0.8**	**25.2**	**0.8**
23_10	**0.0273**	**0.0021**	**0.0039**	**0.0001**	**−0.03**	**257.1**	**9.3**	**0.051**	**0.004**	**0.29**	**27.4**	**2.0**	**25.0**	**0.9**	**24.9**	**0.9**
1_96	**0.0248**	**0.0032**	**0.0036**	**0.0002**	**0.14**	**279.3**	**13.3**	**0.050**	**0.006**	**0.41**	**24.8**	**3.2**	**23.0**	**1.1**	**22.9**	**1.1**
1_69	**0.0197**	**0.0028**	**0.0028**	**0.0001**	**0.31**	**356.1**	**15.2**	**0.051**	**0.007**	**−0.10**	**19.8**	**2.8**	**18.1**	**0.7**	**18.0**	**0.8**
A2-54	$^{207}Pb/^{235}U$	2s	$^{206}Pb/^{238}U$	2s	Err. corr.	$^{206}Pb/^{238}U$	2s	$^{207}Pb/^{206}Pb$	2s	Err. corr.	$^{207}Pb–^{235}U$	2s	$^{206}Pb–^{238}U$	2s	207cor	2s
54_20	0.8150	0.0260	0.0964	0.0031	0.78	10.4	0.3	0.061	0.001	0.52	604.7	14.0	593.0	18.0	NA	NA
54_11	0.6823	0.0210	0.0866	0.0028	0.72	11.5	0.4	0.058	0.001	0.56	528.8	12.0	535.4	17.0	NA	NA
54_21	0.7060	0.0320	0.0859	0.0041	0.91	11.6	0.6	0.060	0.002	0.31	546.0	17.0	534.0	23.0	NA	NA
54_5	0.5670	0.0190	0.0648	0.0024	0.73	15.4	0.6	0.063	0.002	0.54	455.6	12.0	406.2	14.0	NA	NA
54_10	0.0857	0.0030	0.0131	0.0005	0.58	76.5	2.8	0.048	0.001	0.59	83.5	2.8	83.7	3.1	NA	NA
54_16	**0.0680**	**0.0029**	**0.0090**	**0.0003**	**−0.05**	**110.9**	**3.3**	**0.054**	**0.002**	**0.43**	**66.8**	**2.7**	**57.9**	**1.8**	**57.4**	**1.7**
54_7	**0.0575**	**0.0022**	**0.0088**	**0.0003**	**0.44**	**113.5**	**3.6**	**0.048**	**0.002**	**0.01**	**56.7**	**2.1**	**56.5**	**1.8**	**56.5**	**1.8**
A3-15	$^{207}Pb/^{235}U$	2s	$^{206}Pb/^{238}U$	2s	Err. corr.	$^{206}Pb/^{238}U$	2s	$^{207}Pb/^{206}Pb$	2s	Err. corr.	$^{207}Pb–^{235}U$	2s	$^{206}Pb–^{238}U$	2s	207cor	2s
A3_12	4.1200	0.1500	0.2630	0.0099	0.76	3.8	0.1	0.113	0.003	0.34	1656.0	30.0	1504.0	51.0	NA	NA
A3_11	1.3070	0.0420	0.1400	0.0047	0.58	7.1	0.2	0.069	0.002	0.54	848.0	19.0	844.0	27.0	NA	NA
A3_15	0.6560	0.0230	0.0821	0.0030	0.53	12.2	0.4	0.058	0.002	0.60	512.0	14.0	508.0	18.0	NA	NA
A3_20	0.0816	0.0037	0.0106	0.0004	0.46	94.3	3.2	0.056	0.002	0.13	79.6	3.5	68.0	2.3	67.3	2.3
A3_8	**0.0194**	**0.0018**	**0.0028**	**0.0001**	**0.67**	**362.3**	**17.1**	**0.051**	**0.005**	**−0.33**	**19.5**	**1.8**	**17.8**	**0.9**	**17.7**	**0.8**

Bold text – analyses included in the weight mean age estimate; Err. corr. – error correlation between the two preceding isotope ratios. Only estimated for Cenozoic-aged zircons; Discord. – the per cent discordance between the $^{207}Pb–^{235}U$ and $^{206}Pb–^{238}U$ ages; 207cor – the ^{207}Pb corrected age as computed by the software Isoplot, assuming a common $^{207}Pb/^{206}Pb$ ratio of 0.83.

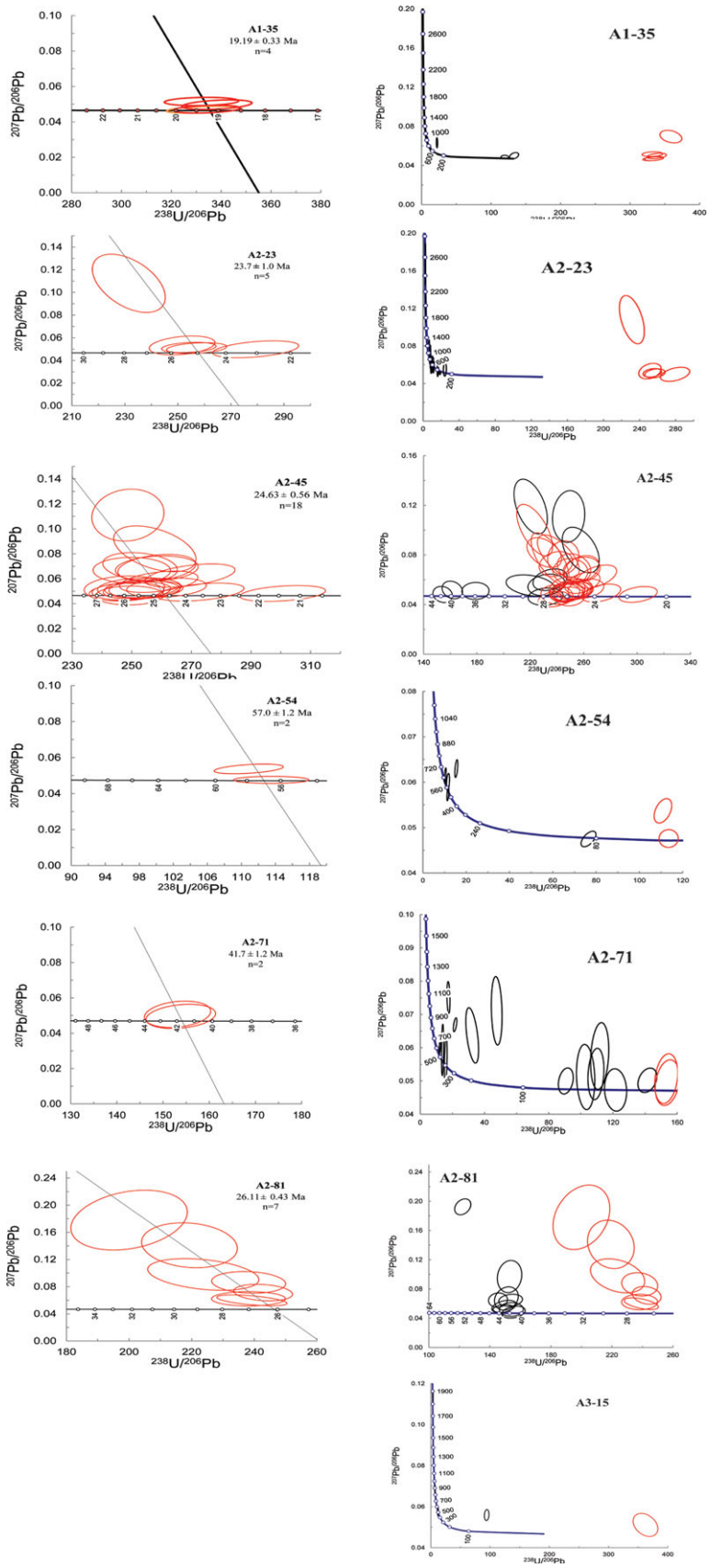

Fig. 4. (Colour online) Inverse Concordia diagrams showing accepted shots for each sample. Preferred U–Pb crystallization ages are computed by a weighted linear fit (thin line) anchored at a 'common' $^{207}Pb/^{206}Pb$ ratio of 0.84 and taking the crystallization age where the linear fit intersects the Concordia line (thick line). Data related to the grains used to estimate the volcanic ages are shown in red.

https://doi.org/10.1017/S0016756820000527 Published online by Cambridge University Press

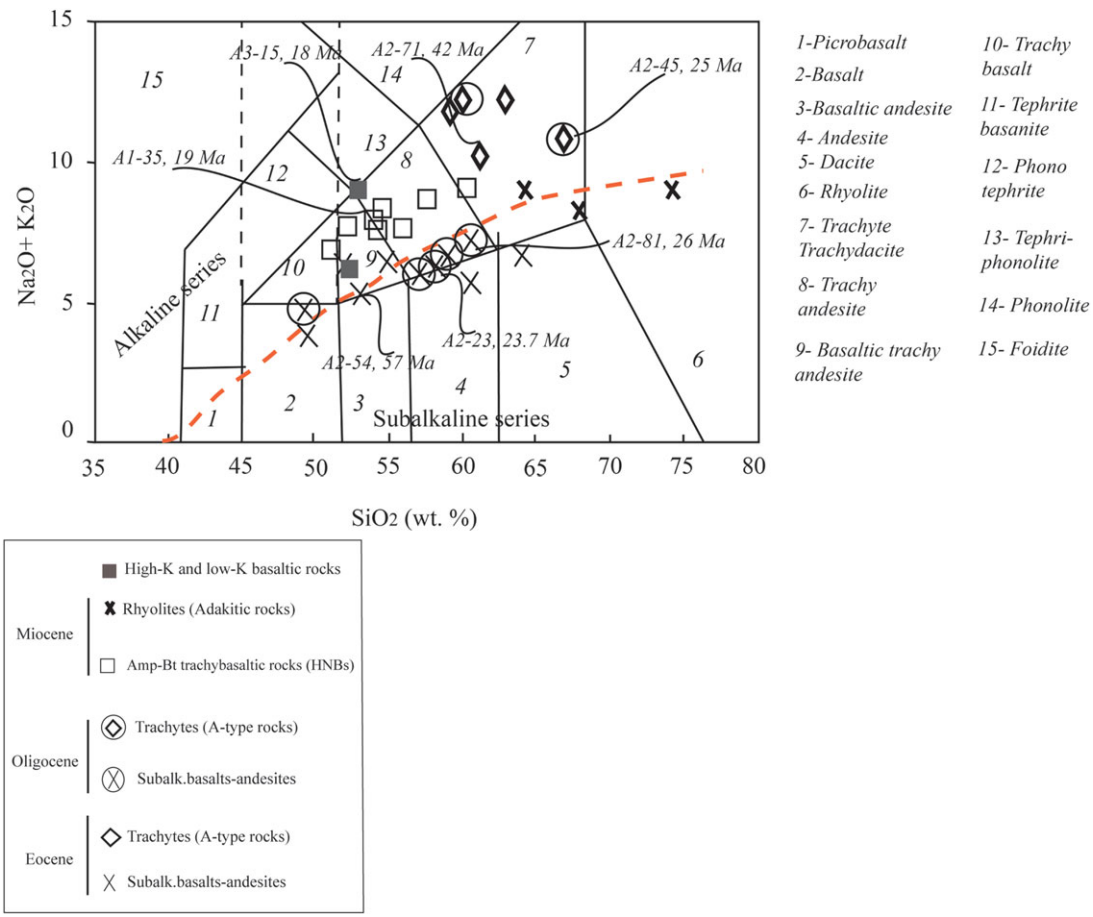

Fig. 5. (Colour online) SE Ahar volcanic rocks encompass a wide compositional range on the TAS (total alkali versus silica) diagram from subalkaline to alkaline and from mafic to felsic rocks. The diagram is after Le Bas *et al.* (1986).

in five samples and encompass wide age ranges. The number of grains dated in each sample is: A3-15 (4 grains), A2-54 (5 grains), A2-23 (20 grains), A1-35 (4 grains) and A2-71 (8 grains). They are mostly late Neoproterozoic to Cambrian (i.e. 22 grains) in age, with a few Palaeoproterozoic zircon ages (i.e. 3 grains). Other inherited zircons include a few with Carboniferous, Devonian, Permian and Cretaceous ages.

4.b. Petrography

4.b.1. Subalkali basalts–andesites

The subalkali basalt–andesite rocks from the study area are porphyritic with a phenocryst mineral assemblage of Cpx ± Pl ± opaque ± Opx ± Ol (online Supplementary Material Fig. S2a, b, c). The groundmass of these volcanic rocks from the study area has essentially the same mineral assemblage as the phenocrysts. Except for olivine and orthopyroxene, which are mostly found as pseudomorphs, in most of the samples, the phenocrysts are mostly fresh and easily recognizable.

4.b.2. Trachytes

The trachytes from the study area mainly include sparse feldspar phenocrysts. The samples contain very few or lack ferromagnesian silicates, amphibole and biotite, either as phenocrysts or in the groundmass that is composed of feldspar microliths, glass and microcrystalline quartz. They are therefore inferred to be felsic and include trachytes. Feldspar microliths appear to demonstrate a preferred orientation in the groundmass of these samples (online Supplementary Material Fig. S2d, e).

4.b.3. Amp-Bt trachybasaltic rocks

The Amp-Bt trachybasaltic rocks show a porphyritic texture. Their phenocryst mineral assemblage comprises Pl + Cpx + opaque ± Amp ± Bt ± Opx (online Supplementary Material Fig. S2f). The groundmass of these rocks has the same mineral assemblage as their phenocrysts. Groundmass feldspar laths show some preferred orientation. Orthopyroxene, amphibole and biotite are partly altered but identifiable. In some samples, the amphiboles and biotites are completely replaced by secondary materials and locally replaced by opaque minerals. Only very rarely are volcanic rocks from the study area recognized to be profoundly altered with epidotization and carbonatization. These were avoided for geochemical analysis.

4.b.4. Rhyolites

The felsic samples (online Supplementary Material Fig. S2g) from SE Ahar are composed of a few feldspar phenocrysts set in a fine-grained leucocratic (i.e. devoid of Fe–Mg silicates and Fe–Ti oxides) groundmass. Some intergranular small quartz microphenocrysts are also present.

4.c. Major and trace elements

Volcanic rocks from the study area are mostly basic–intermediate and clearly separated into distinct alkali and subalkali series on the total alkalis versus silica (TAS) diagram (Fig. 5). The alkali samples

https://doi.org/10.1017/S0016756820000527 Published online by Cambridge University Press

plot across the trachybasaltic–trachyandesitic–trachytic domains, whereas the subalkali samples plot across the basaltic–andesitic–rhyolitic domains. These two series are indistinguishable on some of the major-element Harker variation diagrams (Fig. 6). The alkali rocks contain higher K and Th and lower Mg and Ca than their subalkali counterparts. Nevertheless, on silica versus high field strength element (HFSE) and some other trace-element diagrams (e.g. Hf, Zr, Ta, L, medium REE (MREE)), these two series are neatly separated. On silica versus heavy REE (HREE) diagrams, the alkali and subalkali rocks with up to 60 wt % silica overlap, whereas silica-richer alkali and subalkali rocks show significantly different HREE abundances and patterns.

The most felsic members of the subalkali series (i.e. two rhyolitic and one trachytic sample; Fig. 5) are offset towards higher Na and lower Yb values. They are herein called the low-HREE (i.e. adakitic) series. Basic–intermediate members of the alkali series show high abundances of trace elements, particularly Nb, so they are herein called high-Nb basalts (HNBs). The most felsic members of the alkali series (i.e. five trachytic samples; Fig. 5) show different trace-element abundances and variation trends; owing to their higher alkaline contents as compared to their more basic counterparts, they are herein called A-type rocks.

Although we have thus far described and grouped the rocks in terms of their geochemistry, the subsequent sections group the rocks by the chronological order in which they were erupted.

4.c.1. The Eocene suite

4.c.1.a. The Eocene subalkali basalt–andesite group (~57 Ma). The Eocene subalkali basalts–andesites constitute a bimodal series: four basalts and two andesites separated by a compositional gap. On major-element Harker variation diagrams, they show decreasing variation trends for Fe, Ca, Mg and Al. Normalized trace-element patterns for these rocks show negative Nb–Ta anomalies with high large ion lithophile element (LILE)/HFSE ratios (Fig. 7a). The andesites show trace-element abundances similar to the basalts, except for Rb and Th, which are higher in the andesites, and Sr and Eu, which are lower in the andesites.

4.c.1.b. The Eocene trachytes (A-type rock; ~42 Ma). On most Harker variation diagrams, the Eocene A-type rocks can be distinguished as the higher silica extension of the mafic alkali series. However, the trachytic A-type rocks also show distinctly higher contents of K, Rb and HREEs and lower Sr and Ca as compared to the mafic alkali rocks. The trachytic rocks show a decrease in K, Fe, Ti, Rb and HREEs and an increase in Na, Ba, Eu, Th, Nb, Ta and light REEs (LREEs) with increasing silica. Normalized trace-element patterns for the A-type rocks (Fig. 7b) are distinguished by rather high REE contents, particularly HREEs and HFSEs.

4.c.2. The Oligocene suite

4.c.2.a. The Oligocene subalkali basalt–andesite group (~26 Ma and 24 Ma). The Oligocene subalkali basalts–andesites are mostly andesites with a 55–60 wt % silica range. The andesites show the same Al and Na contents as the Eocene basalts, 1–3 wt % lower CaO, FeO and MgO and 1 wt % higher K_2O. The andesites show slightly higher abundances of all trace elements except Sr as compared to the Eocene basalts. The only Oligocene basalt is more akin to the Oligocene andesites than the basaltic rocks from the study area (i.e. Eocene basalts). The former is richer in trace elements, Na and Al as compared to the latter (c.f. the Oligocene basalt and Eocene basalts at 50 wt % SiO_2).

4.c.2.b. The Oligocene trachytes (A-type rocks; ~25 Ma). The Oligocene trachytes show the same compositional range as the Eocene trachytes that are discussed above (see Section 4.c.1.b).

4.c.3. The Miocene suite

4.c.3.a. The Miocene Amp-Bt trachybasaltic rocks (HNBs; ~19 Ma). The Miocene Amp-Bt trachybasaltic rocks are richer in Sr, Eu, Sm and Nd and poorer in Rb, K and HREEs as compared to the felsic alkali rocks (i.e. trachytes). With increasing Si in the HNBs, Ca, Al, Fe and Ti decrease, whereas alkalis and MgO remain unchanged or increase slightly. The HNBs also shows coherent decreasing MREE–HREE variation trends and coherent increasing Zr, Hf and Th variation trends. Normalized trace-element patterns for the HNBs (Fig. 7e) are characterized by tight clustering and a limited compositional variation. These patterns are also highly enriched in a wide range of trace elements, including immobile trace elements.

4.c.3.b. The rhyolites (adakites; Miocene?). On the majority of the Harker diagrams, the rhyolitic rocks might appear as the more differentiated members of the subalkali basalts and andesites; however, the rhyolitic rocks exhibit higher K and Th and lower HREEs than the basaltic–andesitic rocks. The rhyolites shows a decrease in major elements with increasing silica (i.e. from 64 to 74 wt %), except for K that shows a minimal increase. Most trace elements decrease or remain invariant in the rhyolites, except Th, which shows a modest increase. Normalized trace-element patterns for the rhyolites (Fig. 7f) are identified by their depletion in HREEs. These show rather high LILE contents and low Nb–Ta and La–Ce abundances, with a small negative Nb–Ta anomaly.

4.c.3.c. Other samples: a low-K basaltic rock and a high-K basaltic rock. Two mafic samples from the study area with subalkaline immobile trace-element geochemical affinities show significant differences in LILE abundances (i.e. the inset in Fig. 7a) as compared to the more typical subalkali basalts–andesites. One sample shows exceptionally low LILE contents and lacks a negative Nb–Ta anomaly (i.e. A2-49), which we classify as a low-K basaltic rock. The other mafic sample (i.e. A3-15) is a high-K or LILE-enriched basaltic trachyandesite. This sample plots in the alkali field on the TAS diagram; however, on the normalized trace-element diagram as well as on most Harker diagrams, it is more akin to the subalkali series.

4.d. Sr–Nd isotopic data

Sr and Nd isotopic ratios were determined for a set of ten samples (Table 3) from SE Ahar belonging to the subalkali basalts–andesites (five samples), HNBs (two samples), A-type rocks (two sample) and a high-K basaltic rock (one sample). The initial $^{87}Sr/^{86}Sr$ and $^{143}Nd/^{144}Nd$ isotopic compositions for seven out of ten of these samples were calculated based on their ages obtained by zircon U–Pb dating (Table 4). For the remaining three samples, ages were assigned based on their compositional affinities. Sample A2-26 is a HNB rock, and, as such, it was assumed to have an age of 19 Ma. For the other two samples (A3-18 and A2-84), which belong to the subalkali basalt–andesite group, the calculations were made assuming a value of 26 Ma, because this is the age obtained in this group of samples. The initial Sr ratios vary from 0.704320 to 0.705141 (in A2-54 and A2-84, both from the subalkali basalt–andesite group). The initial Nd isotopic ratios vary from 0.512621 (in A2-84, a subalkali basalt) to 0.512790

https://doi.org/10.1017/S0016756820000527 Published online by Cambridge University Press

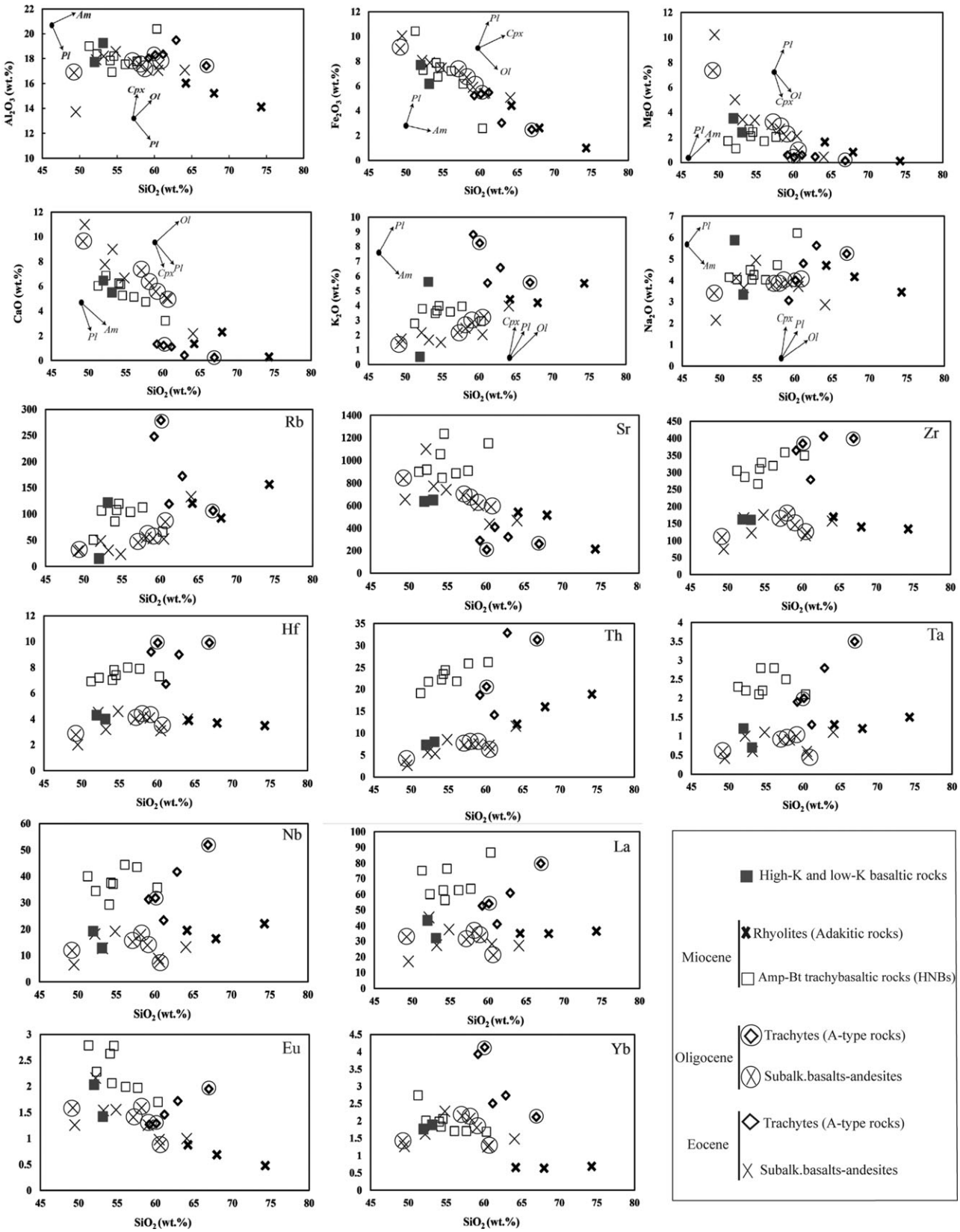

Fig. 6. SiO_2 versus major- and selected trace-element plots for the volcanic rocks from the study area. Arrows demonstrate the differentiation trends likely to develop in the volcanic rocks when fractional crystallization (of the minerals shown) is the responsible mechanism (see text for discussion). Two series of arrows are shown, one is next to the subalkali basalts–andesites, and the other is next to the high-Nb basalts.

https://doi.org/10.1017/S0016756820000527 Published online by Cambridge University Press

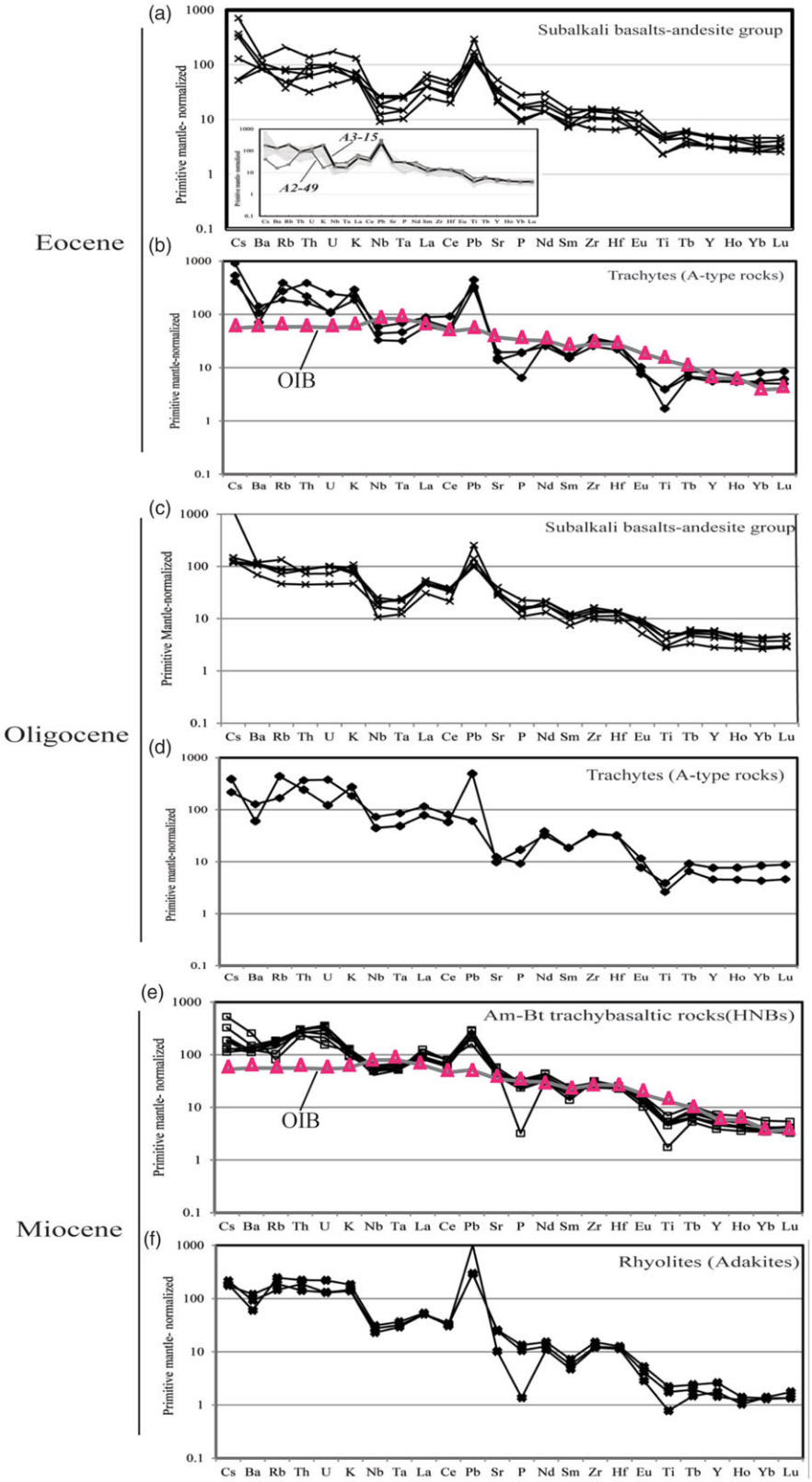

Fig. 7. (Colour online) Primitive-mantle normalized trace-element patterns of different volcanic rock groups from SE Ahar. For explanation of the inset presented in diagram (a), see Section 4.c.3.c. Normalization values are from Sun & McDonough (1989).

https://doi.org/10.1017/S0016756820000527 Published online by Cambridge University Press

(in A1-35, a HNB), which correspond to initial Nd values of 0.0 and +3.4, respectively.

5. Discussion

5.a. Alteration and element mobility

Development of secondary minerals in the volcanic rocks from the study area is strictly limited to a few pseudomorphs after primitive olivine and orthopyroxene (see Section 4.b). This along with LOI values lower than 2.71 wt % in most of the samples (i.e. except the HNBs, one subalkali basalt and one andesite) confirms negligible alteration effects; namely, that the original compositional characteristics of the volcanic rocks have not been obscured by postmagmatic processes (e.g. Yuan *et al.* 2016; Xie *et al.* 2018). Coherent variation in primitive-mantle normalized multi-element patterns of the SE Ahar volcanic rocks indicates the immobility of REEs and HFSEs, thereby confirming original igneous signatures (Polat & Hofmann, 2003). Zr is considered immobile during postmagmatic alteration and is therefore used to monitor element mobility (Pearce *et al.* 1992). Subalkali basalts–andesites and HNBs, which constitute a large number of samples from the study area, demonstrate systematic variation of mobile incompatible elements with Zr (online Supplementary Material Fig. S4), indicating relative immobility of the incompatible elements. This reaffirms that genuine magmatic geochemical signatures are maintained.

5.b. Rock classification

Discussed below in chronological order are the details of the petrogenesis of different groups of volcanic rocks from the study area.

5.c. Eocene subalkali basalts–andesites (~57 Ma)

Olivine and orthopyroxene are common phenocrysts in the basaltic rocks from the study area. These are high-temperature liquidus phases indicating that they are crystallized from primitive-mantle-derived melts. Two other lines of evidence that support the mantle derivation of the subalkaline rocks are: (1) the arc-related trace-element affinity of the subalkaline rocks (online Supplementary Material Fig. S5) and (2) the mantle-derived Sr–Nd isotopic signature of the subalkaline rocks.

5.c.1. Fractional crystallization

The Eocene subalkaline basaltic rocks show low concentrations of compatible elements, Cr and Ni, implying significant differentiation. Steeply decreasing MgO with increasing silica confirms early fractionation of the ferromagnesian silicates olivine and orthopyroxene (Fig. 6). The two andesites from the Eocene subalkaline series show considerably lower Si, Fe, Mg and Ca contents (i.e. as compared to the basalts) at similar Al, alkali, REE and HFSE contents. This may indicate Pl + Cpx + Amp + Ap differentiation, which would have helped buffer trace-element abundance variations.

5.c.2. Source mantle characteristics

The position of the subalkali basalts–andesites on major-element discrimination diagrams such as the K_2O versus silica or the AFM (i.e. Al_2O_3–FeO–MgO) diagram is consistent with the definition of normal calc-alkaline rocks (Fig. 8). The rocks show rather low abundances of highly incompatible immobile trace elements, specifically HFSEs and LREEs–MREEs, so they are akin to the calc-alkaline geochemical characteristics. Most importantly, they are enriched in LILEs and show negative Nb–Ta anomalies (Keppler, 1996; Foley *et al.* 2000). Both of these are well-established signatures of melts created by partial melting in a metasomatized mantle wedge when hydrous fluids and melts released by the subducting slab react with the overlying mantle wedge. This idea is further supported by Sr–Nd data showing that rocks of the basalt–andesite group plot in a region compatible with derivation of their parental melt from a lithospheric mantle (Fig. 9).

Different partition coefficients for REEs in aluminous phases of the upper mantle help estimate the mineralogy of the source mantle (Thirlwal *et al.* 1994; Shaw *et al.* 2003). Garnet prefers HREEs, so garnet-bearing mantle sources produce melts with fractionated REE patterns (i.e. with $Dy/Yb_{(N)} > 2.5$) whereas melts produced by shallower mantle sources, where spinel is stable, show lower $Dy/Yb_{(N)}$ ratios (<1.5; Yang *et al.* 2012). Accordingly, the basaltic–andesitic rocks from the study area are rooted in spinel lherzolite mantle sources. However, using Sm/Yb ratios for modelling mantle partial melting (Aldanmaz *et al.* 2000) suggests a spinel–garnet-bearing mantle source (online Supplementary Material Fig. S6).

5.d. Eocene A-type volcanic rocks (~42 Ma)

SE Ahar trachytic rocks are exceptionally enriched in incompatible trace elements, particularly K, Rb, Th, HFSEs, LREEs, HREEs and Y; therefore, they are considered to represent A-type magmatic rocks. The term 'A-type felsic rocks' is introduced to represent magmatic rocks with characteristic high alkaline abundances, high Ga/Al ratios and enrichments in Nb, Ta, Zr and Hf (Loiselle & Wones, 1979; Collins *et al.* 1982; Whalen *et al.* 1987) (Fig. 10a–d).

The SE Ahar A-type rocks show geochemical signatures atypical of magmatic rocks formed in a subduction-related setting. For example, they (1) lack a negative Nb–Ta anomaly, (2) are exceptionally poor in Ca, Mg and Sr, and (3) show extremely high abundances of K and other incompatible elements. An asthenospheric component is supported by trace-element enrichment (particularly high Nb–Ta) and normalized trace-element patterns similar to those of ocean island basalts (OIBs) (Fig. 7b). The A-type magmatic rocks indicate within-plate geochemical characters and are believed to have been commonly emplaced in an extensional geodynamic setting, either related to continental rift zones (i.e. anorogenic A-type rocks) or post-collision extensional regimes or continental arc to back-arc extension (Whalen *et al.* 1987; Eby, 1992; Turner *et al.* 1992; Dargahi *et al.* 2010).

The binary A_1–A_2 classification scheme for A-type magmatic rocks is intended to reflect their contrasting origins and tectonic settings (Eby, 1992). The A_1-subtype shows intraplate OIB geochemical characteristics, whereas the A_2-subtype shows island arc affinity. A-type samples from the study area plot at the boundary between the A_1 and A_2 subtypes (Fig. 10e), though a few of them tend towards the A_1-domain. It seems as if the SE Ahar A-type samples show compositions intermediate between the A_1 and A_2 subtypes. This feature is supported by the SE Ahar A-type samples forming a compositional array between the OIB and island arc basalt (IAB) end-members (Fig. 10f) representing asthenospheric mantle and lithospheric mantle, respectively. Hence, a mixed asthenospheric–lithospheric mantle source is suggested to have supplied the parental magma for the A-type rocks. FeO/(FeO + MgO) ratios of these samples from the study area furnish further support for this hypothesis since the SE Ahar A-type rocks plot in the overlapping area of the reduced and oxidized subgroups (Fig. 10g) of A-type rocks

https://doi.org/10.1017/S0016756820000527 Published online by Cambridge University Press

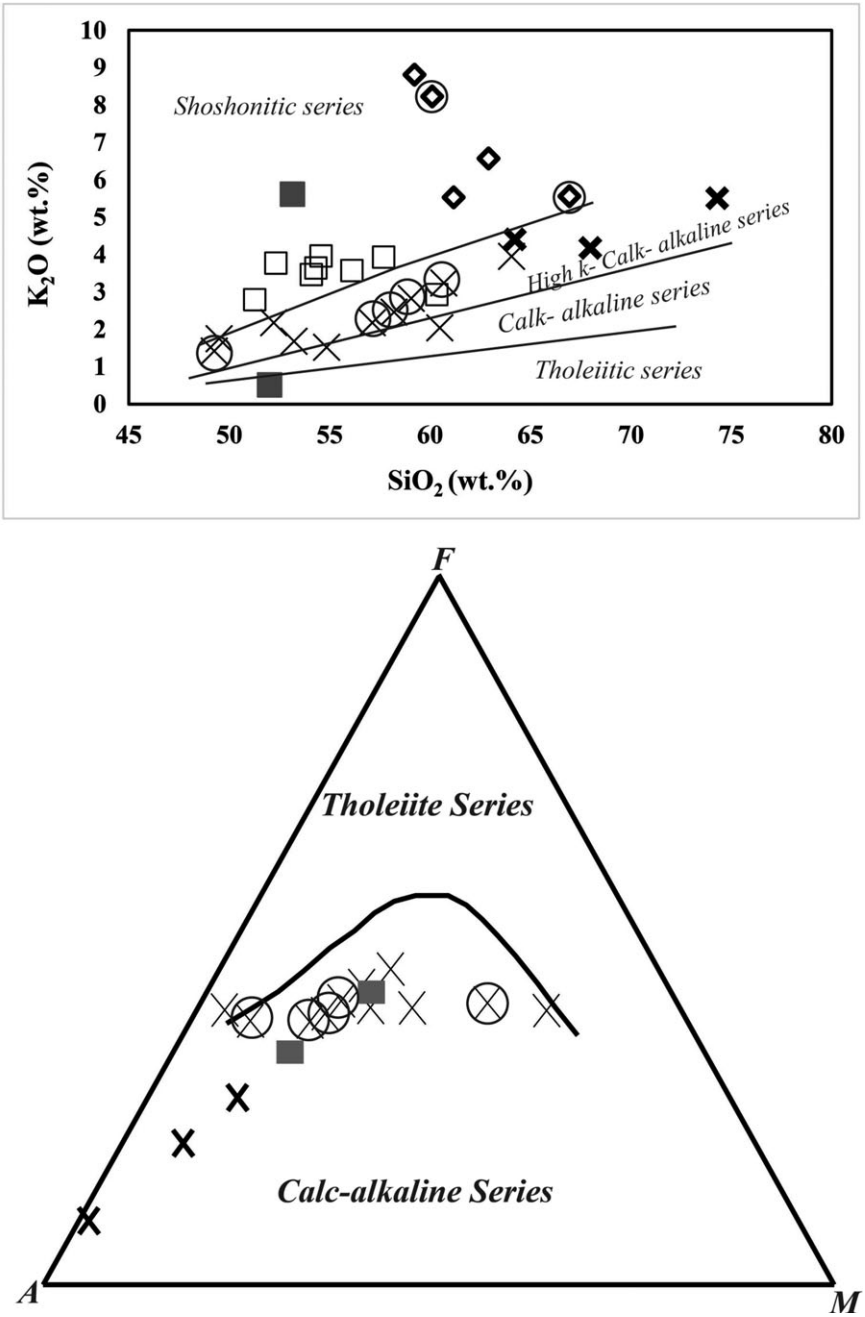

Fig. 8. Subalkaline rocks from the study area, mainly subalkali basalts–andesites (see TAS diagram, Fig. 5), plot in the calc-alkaline domain on the K_2O versus SiO_2 and AFM (Al_2O_3–FeO–MgO) diagrams. Diagrams after Peccerillo & Taylor (1976) and Irvine & Baragar (1971), respectively. Symbols as in Figure 5.

(Anderson & Morrison, 2005; Dall'Agnol & Oliveira, 2007). OIBs are usually evolved under conditions of lower H_2O contents than IAB; these correspond to the reduced and oxidized subgroups, respectively.

In order to introduce an asthenospheric mantle component in subduction-related settings, slab break-off (Davies & von Blanckenburg, 1995; Wang *et al.* 2018) or slab roll-back (Okay & Sahinturk, 1997; Boztug & Harlavan, 2008; Kaygusuz *et al.* 2008; Verdel *et al.* 2011) have been suggested as the two major trigger mechanisms. Based on the sequences of events recognized in the study area, however, the slab roll-back mechanism is preferred here. A-type rocks from the study area are dated to ~42 Ma. These pre-date the HNBs that are dated to ~19 Ma (i.e. considered to represent slab break-off; see below). With increasing silica in the A-type rocks, they develop a negative P anomaly and their negative Ti anomaly deepens. These are associated with increasing Na, Ba, U–Th, Nb–Ta and LREEs and decreasing K, Rb and HREEs. It is thus likely that fractional crystallization of feldspar + opaque + apatite + a HREE-enriched accessory phase led to the variation trends observed in the A-type rocks from the study area.

5.e. Oligocene subalkali basalts–andesites (~26 and 24 Ma)

The Oligocene subalkaline basic rocks are mainly andesitic with Fe and Mg abundances similar to the Eocene basaltic rocks. The Oligocene andesites do not follow curved variation trends as observed for the more basic rocks (i.e. mainly Eocene basalts).

https://doi.org/10.1017/S0016756820000527 Published online by Cambridge University Press

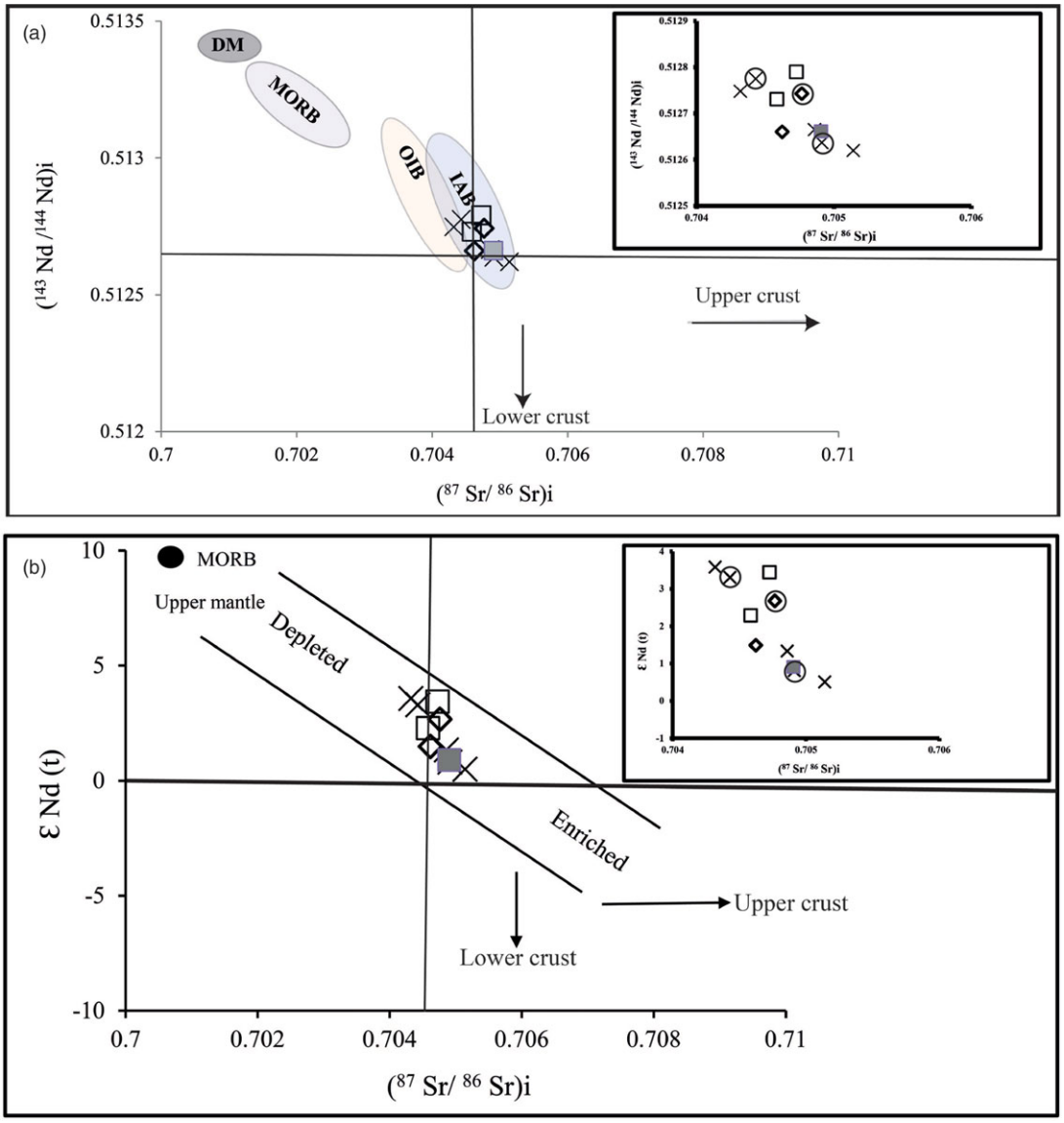

Fig. 9. (Colour online) (a) Initial Sr–Nd isotopic ratios are shown for representative samples from different groups of SE Ahar volcanic rocks. Domains for depleted mantle (DM), ocean island basalts (OIB) and island arc basalts (IAB) are after Zindler & Hart (1986). (b) $Nd_{(t)}$ versus initial Sr isotopic ratio for SE Ahar volcanic rocks. Symbols as in Figure 5.

This rules out their differentiation from the basalts. Hence, the andesites are inferred to represent primitive melts. Trace elements and Sr–Nd isotopic signatures of the Oligocene andesites as compared to arc-related affinity settings support the derivation of their primitive melts from a lithospheric mantle (Fig. 9; online Supplementary Material Fig. S5). Higher Si and slightly higher alkalis and incompatible trace-element abundances in the andesites imply a moderately richer mantle source as compared to the Eocene basaltic rocks (Zindler & Hart, 1986; Müller & Groves, 1995; Marquez *et al.* 1999). Higher fusible mineral contents (e.g. Cpx, Sp, Opx) and/or higher trace-element abundances of the fusible minerals in the source mantle help to develop such enriched mantle signatures (Pickering-Witter & Johnston, 2000). The Oligocene basaltic rock shows geochemical characteristics more akin to the Oligocene andesites (see Section 4.c.2.a). The low Si content of this sample as compared to the Oligocene andesites might be due to the olivine cumulative nature of this sample (i.e. A3-14).

5.f. Oligocene A-type rocks (~25 Ma)

The Oligocene A-type rocks have a similar compositional range to the Eocene A-type rocks and are inferred to have originated and evolved by the same petrogenetic processes as presented in the geodynamic model section (see Section 7 below).

5.g. Miocene high-Nb basalts (HNBs; ~19 Ma)

Basaltic trachyandesites with high Nb abundance (i.e. Nb >20 ppm) from the study area are defined as HNBs (Defant *et al.* 1992). These were found to represent a within-plate and arc-related geochemical signature. Various HNBs with positive to negative Nb–Ta anomalies on primitive-mantle normalized trace-element patterns (Fig. 7e) have been recognized in different arc-related settings and interpreted as OIB-like components in an arc geodynamic framework. Hastie *et al.* (2011) believed that HNBs are basic melts with an intraplate signature generated in subduction zones (Fig. 11a, b); they were attributed to either

https://doi.org/10.1017/S0016756820000527 Published online by Cambridge University Press

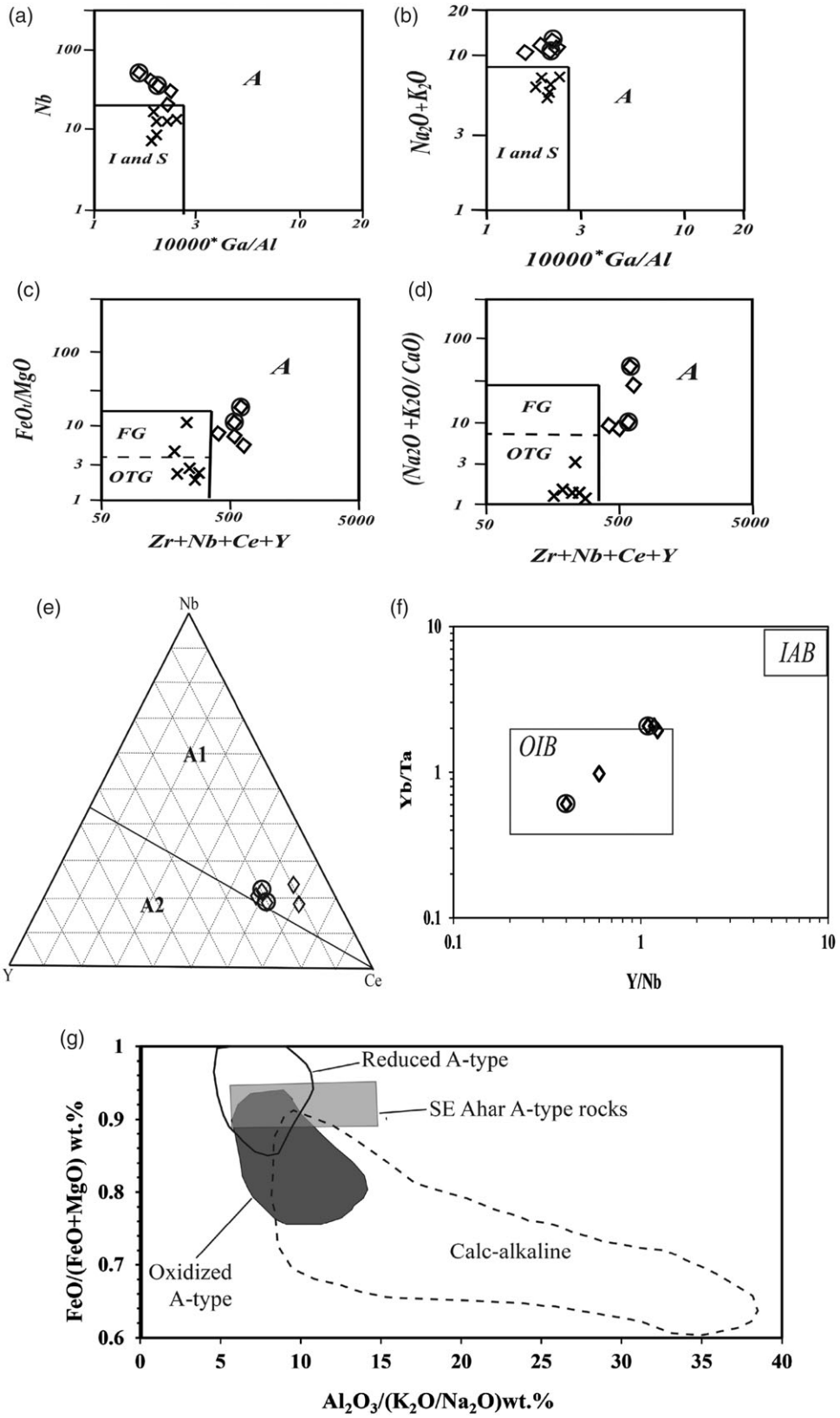

Fig. 10. Felsic rocks from the study are shown on (a) Nb versus 10000* Ga/Al; (b) $Na_2O + K_2O$ versus 10000* Ga/Al; (c) FeO/MgO versus Zr + Nb + Ce + Y; (d) ($Na_2O + K_2O$/CaO) versus Zr + Nb + Ce + Y diagrams. (e) Nb–Y–Ce ternary diagram discriminating between A_1 and A_2 subtypes. (f) Yb/Ta versus Y/Nb diagram discriminating between OIB-affinity and IAB-affinity rocks. (g) FeO/(FeO + MgO) wt % versus Al_2O_3/(K_2O/Na_2O) wt % diagram discriminating between oxidized A-type and reduced A-type rocks. These geochemical diagrams discriminate A-type magmatic rocks (SE Ahar trachytes) from other types (i.e. igneous, sedimentary and mantle types). These diagrams are usually used for granitic rocks. FG – fractionated granites; OTG – unfractionated granites. Domains shown for diagrams (a) to (d) are after Pearce *et al.* (1984) and Whalen *et al.* (1987), (e) and (f) are after Eby (1992) and (g) is after Dall'Agnol & Oliveira (2007). Symbols as in Figure 5.

https://doi.org/10.1017/S0016756820000527 Published online by Cambridge University Press

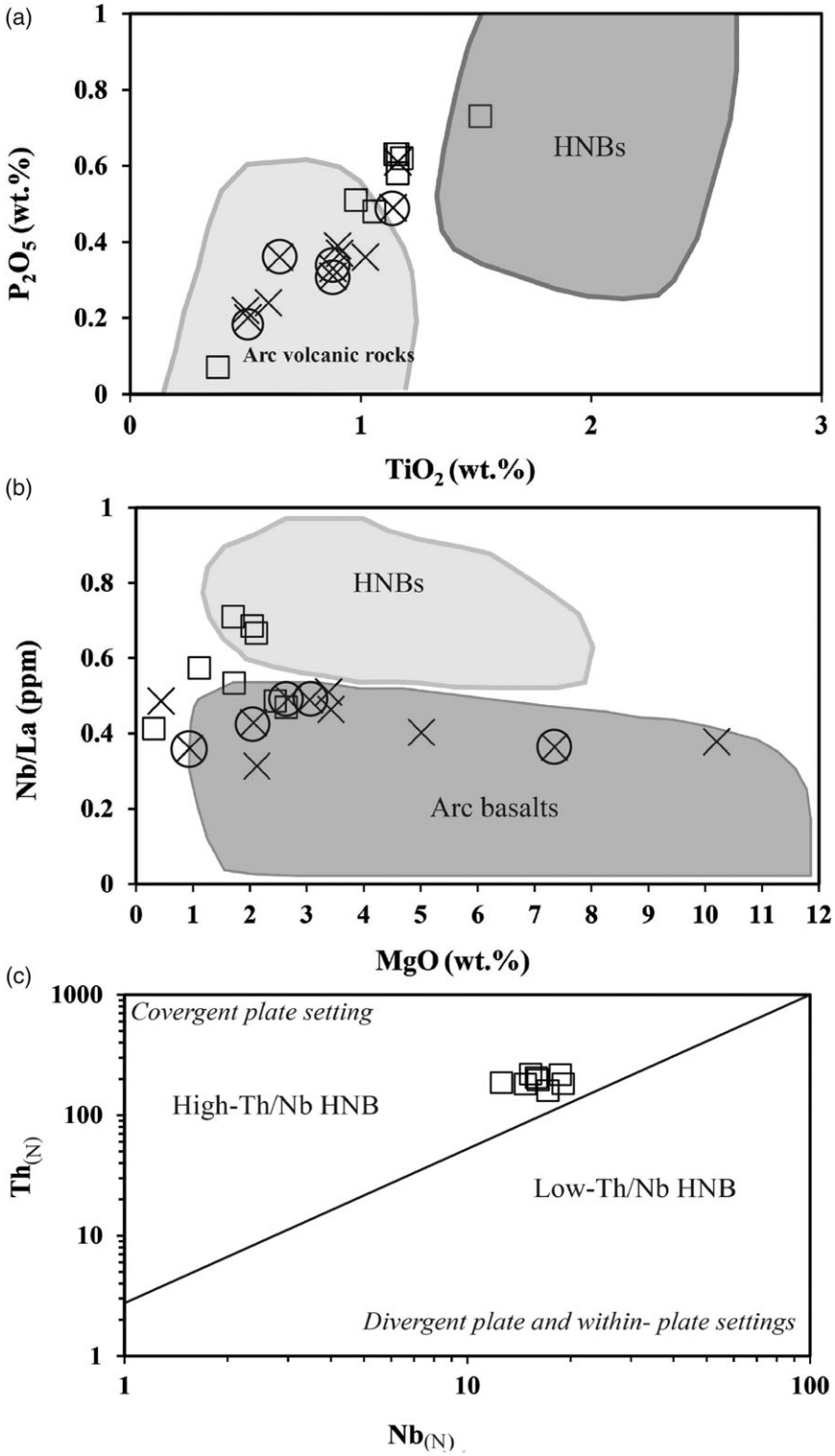

Fig. 11. (a) P_2O_5 versus TiO_2 plot; (b) Nb/La ratio versus MgO plot; and (c) Th_N versus Nb_N diagram for SE Ahar mafic volcanic rocks that distinguishes high-Nb basaltic rocks (HNBs) from arc volcanic rocks (after Saccani, 2015). HNBs and arc volcanic domains are after Defant *et al.* (1992). Symbols as in Figure 5.

(1) mantle wedge metasomatized by slab melts or (2) mixing products of an enriched (OIB-type) and a depleted (mid-ocean ridge basalt (MORB)-type) source mantle.

The generation of HNBs in subduction settings is often attributed to either a mantle plume origin or a metasomatized mantle wedge (Reagan & Gill, 1989; Castillo *et al.* 2007). The mantle plume involvement (first hypothesis) is based on the compositional similarity of HNBs and OIB (Verma & Nelson, 1989; Castillo *et al.* 2002). We do not favour this hypothesis, because HNBs from the study area are not as rich in Nb and Ti as OIB, and their Sr–Nd isotopic values show no significant distinction from other volcanic rocks in the study area (Fig. 9).

https://doi.org/10.1017/S0016756820000527 Published online by Cambridge University Press

Instead we favour the second hypothesis, that the HNBs were derived from a metasomatized mantle wedge wherein the interaction between the mantle wedge and slab melts generates HFSE-rich mineral assemblages (Defant & Drummond, 1993; Sajona *et al.* 1993, 1996; Zhang *et al.* 2005). This idea is supported by the high Sr/Y ratios of the high-Nb rocks, suggesting that the slab melts formed at high pressure. However, such a model would predict the existence of classic 'slab-derived' adakites in the study area. One explanation for their absence is that any slab melts formed were consumed in reaction with the mantle.

A significant oceanic crustal (slab) contribution in the petrogenesis of the high-Nb basaltic rocks from SE Ahar is implied by their high LOI abundances. Oceanic crust is well known for its hydrated nature and its involvement in the origin of HNBs, culminating in a high LOI content of the partial melt produced. High and low Th/Nb ratios were proposed as diagnostic identifiers of the petrogenesis of HNBs (Fig. 11c). High Th/Nb distinguishes convergent plate settings while low Th/Nb specifies divergent plate and within-plate settings. The SE Ahar volcanic rocks on these diagrams plot near the boundary between these two settings, with the majority of data plotting in the convergent plate domain.

Ca, Fe and K variation trends in the HNBs from the study area mimic the subalkali basalt–andesite compositional variation. However, the HNBs show decreasing Al and slightly increasing Mg variation trends that are different from the subalkaline series variation trends. A plagioclase + amphibole-dominated fractional crystallization appears to reasonably match the HNB compositional range. A major role for amphibole fractionation is particularly supported by decreasing MREE abundances in the HNBs from the study area. The petrography, too, is consistent with such a finding, because amphibole and plagioclase are ubiquitous phases in the HNBs from the study area.

5.h. Rhyolites (adakites)

The rhyolites plot in the trachyte and rhyolite fields at the boundary between the alkaline and subalkaline series. The rhyolitic group is characterized by its lower HREE and Ca contents and higher Na as compared to the normal calc-alkaline rocks. These geochemical characteristics generally match the compositional signatures of adakites (Fig. 12a, b).

Adakites are regarded as subducted oceanic slab partial melts under high pressure where an omphacite and garnet ± amphibole mineral assemblage substitutes MORB (Rapp & Watson, 1995; Prouteau *et al.* 2001). The oceanic slab partial melt is highly enriched in Sr and depleted in HREEs. Martin *et al.* (2005) classified adakites into high-silica and low-silica types. Adakite rocks from the study area are the high-silica (HSA) type (Fig. 12c), implying that they have not been derived from source regions that were reacted with the source mantle (Wang *et al.* 2017). The low contents of MgO and other incompatible elements confirm this finding.

Primarily, adakites were defined as the product of partial melting of subducted young, hot, flat oceanic slabs (Defant & Drummond, 1990). Other models proposed to account for the petrogenesis of adakitic rocks include partial melting of thickened mafic lower crustal rocks (Atherton & Petford, 1993; Yogodzinski *et al.* 1995; Petford & Atherton, 1996; Chung *et al.* 2003; Hou *et al.* 2004; Chiaradia, 2009; Kamei *et al.* 2009) or high-pressure fractional crystallization from a mafic melt derived from mantle wedge peridotite (Muntener *et al.* 2001; Alonso-Perez *et al.* 2009; Chiaradia, 2015).

Although low HREE concentrations suggest classification as adakites, samples from the study area lack the Sr enrichment expected in typical adakites. The latter are derived from subducted oceanic slab melts at the high pressure of eclogite facies where plagioclase is unstable. High Th (Fig. 13a) and K abundances (Fig. 13b, c) in the SE Ahar adakites also make them akin to adakites derived from crustal rocks. Plagioclase might be considered as a residual phase in the crustal rocks. Plagioclase shows high partition coefficients (Kds) for Sr (>2; Blundy *et al.* 1998), so its presence in the crustal source rocks could lead to the Sr decrease in the induced adakite partial melt. High Sr isotopic ratios for the rhyolites would support this hypothesis. Isotopic data were not obtained for the rhyolitic rocks. Citing a relatively thin lithosphere (i.e. of 100 km thickness) and a rather thickened crust of 38.5–48 km for NW Iran, Lechman *et al.* (2018) suggested that asthenospheric ascent prompted thermal erosion of the lithospheric mantle, delamination of mantle slivers and a crustal lithospheric component. The latter idea of crustal delamination is consistent with a crustal source for the SE Ahar adakitic rocks.

Rhyolitic rocks from the study area with adakitic characteristics could be formed by fractional crystallization of the more basic members of the volcanic succession described here. These rhyolites plot along a high-pressure differentiation trend on Figure 14. High-pressure fractional crystallization that mainly includes amphibole and garnet (Hidalgo *et al.* 2011) is expected to develop systematic Dy/Yb variation. However, the scarcity of amphibole phenocrysts in the rhyolitic rocks and the lack of a significant MREE negative anomaly does not support this hypothesis as the major process that led to the development of the adakitic characteristic of the SE Ahar rhyolitic rocks. Partial melting of lower crustal rocks appears to be the more acceptable alternative for the origin of the rhyolitic rocks.

5.i. The low-K basaltic rock and high-K basaltic rock

These are immobile trace-element poor volcanic rocks with contrasting LILE abundances. These rocks from the study area include two basaltic rocks, samples A3-15 and A2-49. The former is unique in the study area because, despite typical subduction characteristics (i.e. a high LILE/HFSE ratio), it is highly K enriched. It approaches the tephriphonolite field on the TAS diagram. This K-rich basaltic rock, which is of the same age as the HNBs from the study area (i.e. A1-35), is probably derived from a highly metasomatized part of the mantle wedge containing a higher amount of amphibole and phlogopite.

The latter sample from the study area (i.e. A2-49) apparently lacks the negative Nb–Ta anomaly that characterizes subduction-related magmatic rocks. However, its Nb–Ta abundances and its high LILE/HFSE ratios overlap those of subalkaline subduction-related melts. In fact this sample with low-K (i.e. tholeiitic) affinity is likely to represent the earlier stage of subduction-related magmatism in the region.

6. Degree of crustal contamination

Occurrence of a wide variety of magmatism in the study area in a rather short period of time (namely, 41–18 Ma) is an enigmatic aspect of the present study. This period of time coincides with events previously interpreted to be amplified or initial collisional events (e.g. Agard *et al.* 2005; Vincent *et al.* 2005; Ballato *et al.* 2011; van Huen & Allen, 2011). Initial collisional magmatism was likely triggered by a variety of mechanisms that include slab

https://doi.org/10.1017/S0016756820000527 Published online by Cambridge University Press

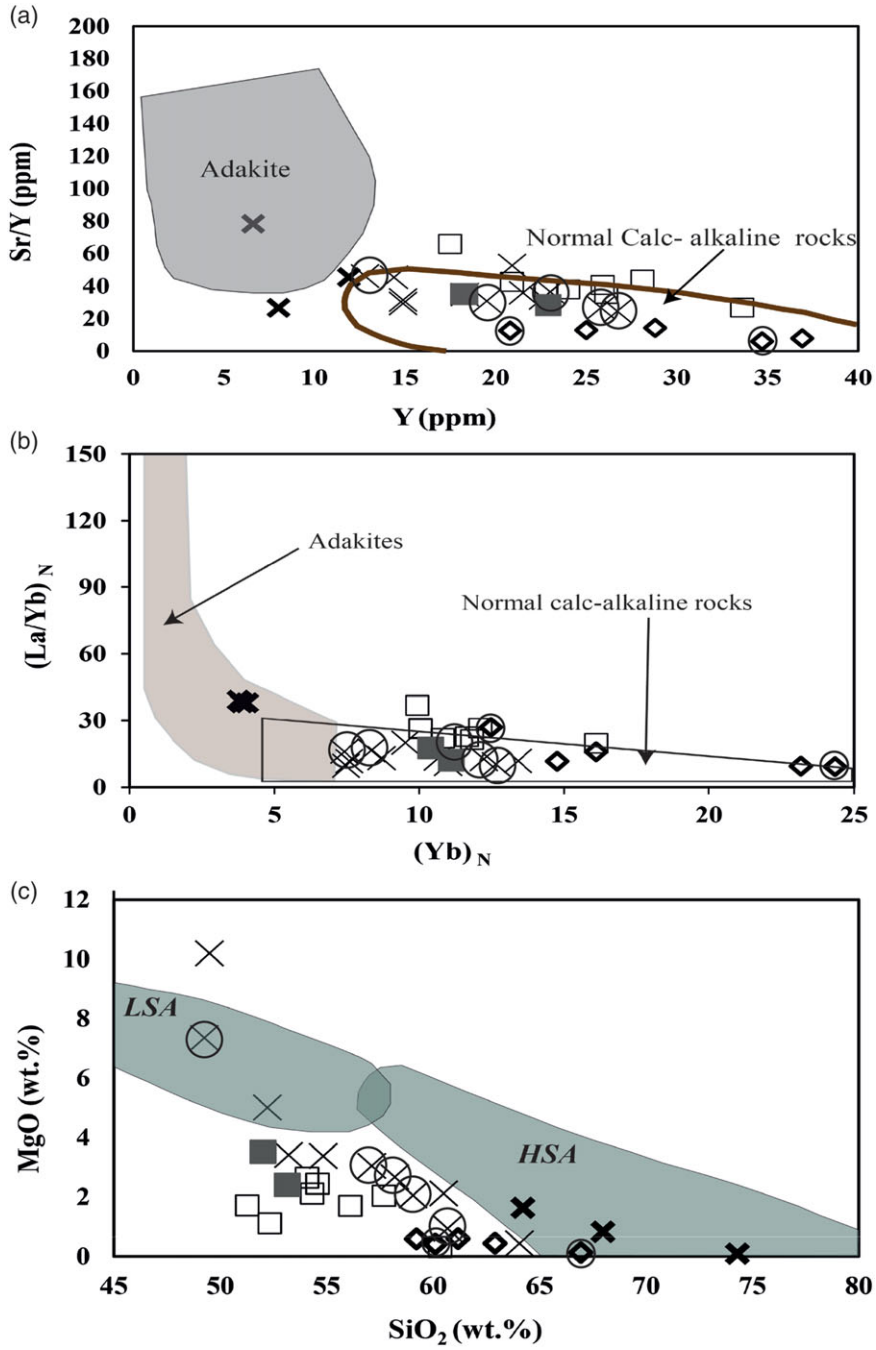

Fig. 12. (Colour online) Rhyolitic rocks from SE Ahar tend towards the adakitic domain on (a) Sr/Y versus Y (domains are after Defant *et al.* 1991; Defant & Drummond, 1990 and Martin *et al.* 2005) and (b) $(La/Yb)_N$ versus Yb_N (Defant & Drummond, 1990; Petford & Atherton, 1996) diagrams. (c) MgO versus SiO_2 diagram for classifying adakites into high-silica adakites (HSA) and low-silica adakites (LSA) after Martin *et al.* (2005). Adakitic rocks from SE Ahar plot in the HSA domain. Symbols as in Figure 5.

break-off and delamination or thinning of the lithospheric mantle (Neill *et al.* 2015 and references therein). In addition to these processes, crustal contributions appear significant for some units. For example, the presence of inherited zircons in the SE Ahar volcanic rocks confirms some extent of crustal contamination. Inherited zircons in the subalkali basalts–andesites (i.e. three samples, A2-54, A2-23 and A2-81) and HNBs (i.e. one sample, A1-35) from the study area are restricted to late Palaeozoic–Precambrian basement zircons, whereas in the SE Ahar A-type volcanic rocks, they are mainly in the Palaeozoic–Mesozoic age range. Late Neoproterozoic – early Cambrian ages imply a hidden crustal basement for NW Iran, which is similar to the UDMA and Sanandaj–Sirjan Zone. These may be derived from rocks of the Cadomian orogeny (Ramezani & Tucker, 2003; Rahmati-Ilkhchi *et al.* 2011) or amalgamation of NE Gondwana and the South China Block (Stampfli *et al.* 2013; von Raumer *et al.* 2015). A few Palaeoproterozoic zircons indicate the incorporation of older crustal materials (i.e. those derived from the African craton and supplied by Central Iran sedimentary beds) in the late Neoproterozoic – early Cambrian magmatism (Chaharlang & Ghorbani, 2020). The presence of 1870 Ma detrital zircons in the Tashk Formation siliciclastic rocks (Ramezani & Tucker,

https://doi.org/10.1017/S0016756820000527 Published online by Cambridge University Press

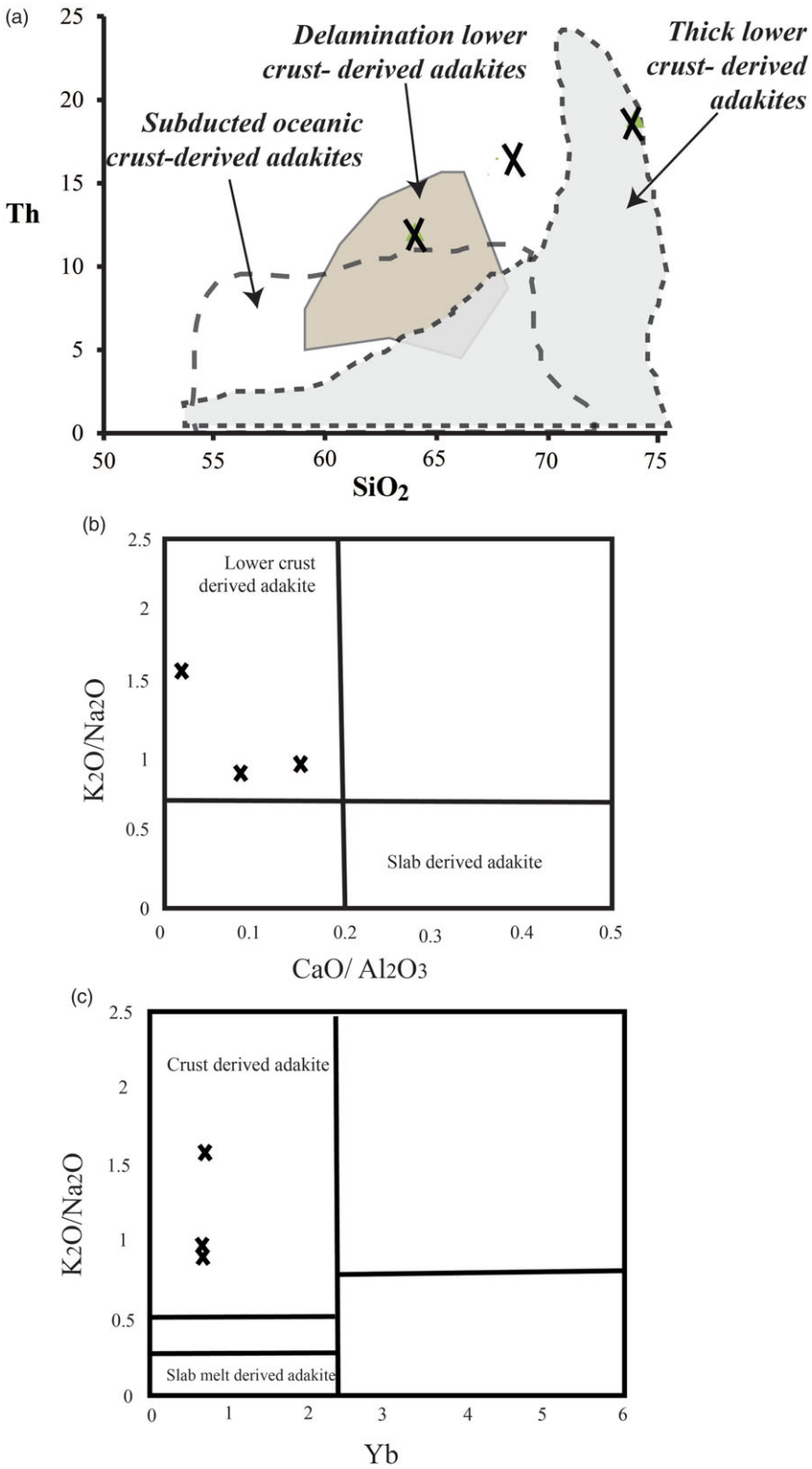

Fig. 13. (Colour online) Geochemical identification diagrams that help distinguish crustal-derived adakitic rocks from slab-derived adakites. (a) Th versus silica plot (after Wang *et al*. 2006 and references therein); (b) K_2O/Na_2O versus CaO/Al_2O_3 (after Li *et al*. 2016 and references therein), and (c) K_2O/Na_2O versus Yb plot (after Kamvong *et al*. 2014 and references therein). Symbols as in Figure 5.

https://doi.org/10.1017/S0016756820000527 Published online by Cambridge University Press

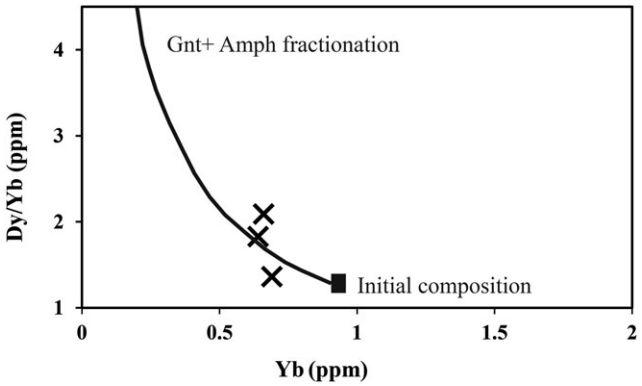

Fig. 14. High-pressure differentiation trend that mainly involves garnet + amphibole fractionation (Hidalgo *et al.* 2011) is shown along with the rhyolitic rocks (adakites) from SE Ahar. Symbols as in Figure 5.

2003) and their equivalent in N and W Iran, the Kahar Formation, indicates they could be the source of old xenocrystic zircons in the magmatic rocks. Alternatively, a hidden, subsurface Mesoproterozoic and Palaeoproterozoic magmatic source might be present. The zircons straddling the Carboniferous are regarded as being derived from the Eurasian arc, which resulted from Palaeotethyan oceanic plate subduction towards the north. The Cretaceous zircons indicate a Late Cretaceous magmatic episode that followed Neotethyan subduction (Chaharlang & Ghorbani, 2020).

Another line of evidence for crustal contamination is high Th/La ratios in the SE Ahar HNBs (i.e. higher than former estimates of the Th/La ratios for Iranian magmatic rocks; see fig. 12 in Neill *et al.* 2015) that approach crustal values (Plank, 2005), indicating a high degree of crustal contamination. Nevertheless, the SE Ahar subalkali basalts–andesites show relatively low Th/La ratios. High Th/La ratios in the HNBs might partly be due to the contribution of subducting slab partial melts that included oceanic sedimentary components.

7. Geodynamic evolution

Zircon U–Pb ages obtained for the volcanic rocks from the study area are integrated with the geochemical data to reconstruct the magmatic and geodynamic evolution; these are introduced here for the four groups of rocks. (1) The subalkali basalts–andesites present three ages, 57.0 ± 1.2 Ma, 23.7 ± 1.0 Ma and 26.1 ± 0.4 Ma. (2) The A-type rocks present two ages, 41.7 ± 1.2 Ma and 24.6 ± 0.6 Ma. (3) The HNBs present one age, 19.2 ± 0.3 Ma. (4) The adakitic rocks, owing to the low number of zircon grains retrieved, have not been age dated. The unique high-K basaltic sample appears to be 18 Ma in age, although this is based on a single zircon age. Except for its high potassium content, this basaltic sample is of the same geochemical characteristics as the subalkali basalts–andesites.

The subalkali basalts–andesites show explicit subduction-related signatures and settings. The A-type rocks and the HNBs are also closely affiliated with such settings (see Section 5 above). The U–Pb ages of these subduction-derived magmatic rocks allow speculation on whether they formed during a synorogenic or postorogenic phase of tectonism. Four samples with subduction-related signatures are dated as ~57 Ma, 26 Ma, 24 Ma and 18 Ma. Former studies on magmatic rocks from NW Iran reported similar ages of 53 Ma (Hassanzadeh *et al.* 2008), 25 Ma and 23 Ma (Aghazadeh *et al.* 2010, 2011) for rocks with subduction-related signatures. These overlap temporally with samples from this study, which show the unprecedented geochemical signatures of A-type trachytic (~42 Ma and 25 Ma) and Nb-enriched basaltic rocks (~19 Ma), both well known for representing postorogenic and/or extensional conditions and settings (Zhao *et al.* 1996; Han *et al.* 1997; Jahn *et al.* 2000*a*,*b*; Wu *et al.* 2000, 2002; Liu, 2002; Liu & Fei, 2006; Castillo, 2008; Macpherson *et al.* 2010). Therefore, it appears that near ~42 to 19 Ma both the mantle wedge and the asthenospheric mantle underwent concurrent partial melting. Asthenospheric mantle influx likely occurred through slab roll-back. Magmatic rocks with 37–42 Ma ages with an asthenospheric signature (Nabatian *et al.* 2014) as well as magmatic rocks with 38–39 Ma ages with subduction-related signatures (Castro *et al.* 2013) have been reported from NW Iran.

The results presented here are consistent with a model in which northeastward subduction of the Neotethyan oceanic slab gradually slowed, eventually prompting slab retreat followed by decompression melting and emplacement of the UDMA beginning in Eocene time (Fig. 15). Our results suggest that tholeiitic to calc-alkaline mafic melts and their differentiation products represent slab-fluid driven metasomatized mantle melting. Importantly, we show that this subalkaline magmatism in the SE Ahar area spans the Eocene to Late Miocene period (Fig. 15). We argue that asthenospheric mantle influx triggered by continued slab roll-back supplied the source material for the Early Miocene A-type melts that produced the trachytic rocks in SE Ahar. Further slab retreat and steepening exposed the slab to the higher temperatures and pressures of the asthenospheric mantle, which culminated in slab partial melting. The deep slab partial melts penetrated into and metasomatized the lithospheric mantle, thereby furnishing the source material for the Late Miocene HNBs in SE Ahar. Elevated temperature gradients imposed by the Late Miocene events might have induced lower crustal partial melting that produced the adakitic melts, which may be the youngest volcanic rocks in the suite.

This model is compatible with the timing/succession of asthenosphere-derived component emergence in the UDMA and AMA. Slab roll-back propagated westward (i.e. from the AMA towards the UDMA), so the asthenosphere influx underlying the AMA should have pre-dated the UDMA. A Late Eocene (i.e. 41 Ma) age for the A-type volcanic rocks from SE Ahar and an Oligocene (i.e. 25 Ma) age for the OIB-type rocks from the UDMA (Verdel *et al.* 2011; Ghorbani *et al.* 2014) seem consistent with the development of an enriched plume-type signature as roll-back proceeded towards the west. Higher alkaline and trace-element contents of the volcanic rocks from the AMA as compared to the UDMA are also compatible with the expected spatial distribution of arc magmatism. Both increasing continental crustal thickness towards the east (i.e. from the UDMA towards the AMA) and a likely back-arc position of the AMA are consistent with evolution of arc magmatism towards more alkaline affinities. Owing to the deeper slope of the slab beneath the AMA, slab melt metasomatism and subsequent HNB formation occurred here while it is absent in the UDMA. Ultimately, slab roll-back probably culminated in slab break-off.

https://doi.org/10.1017/S0016756820000527 Published online by Cambridge University Press

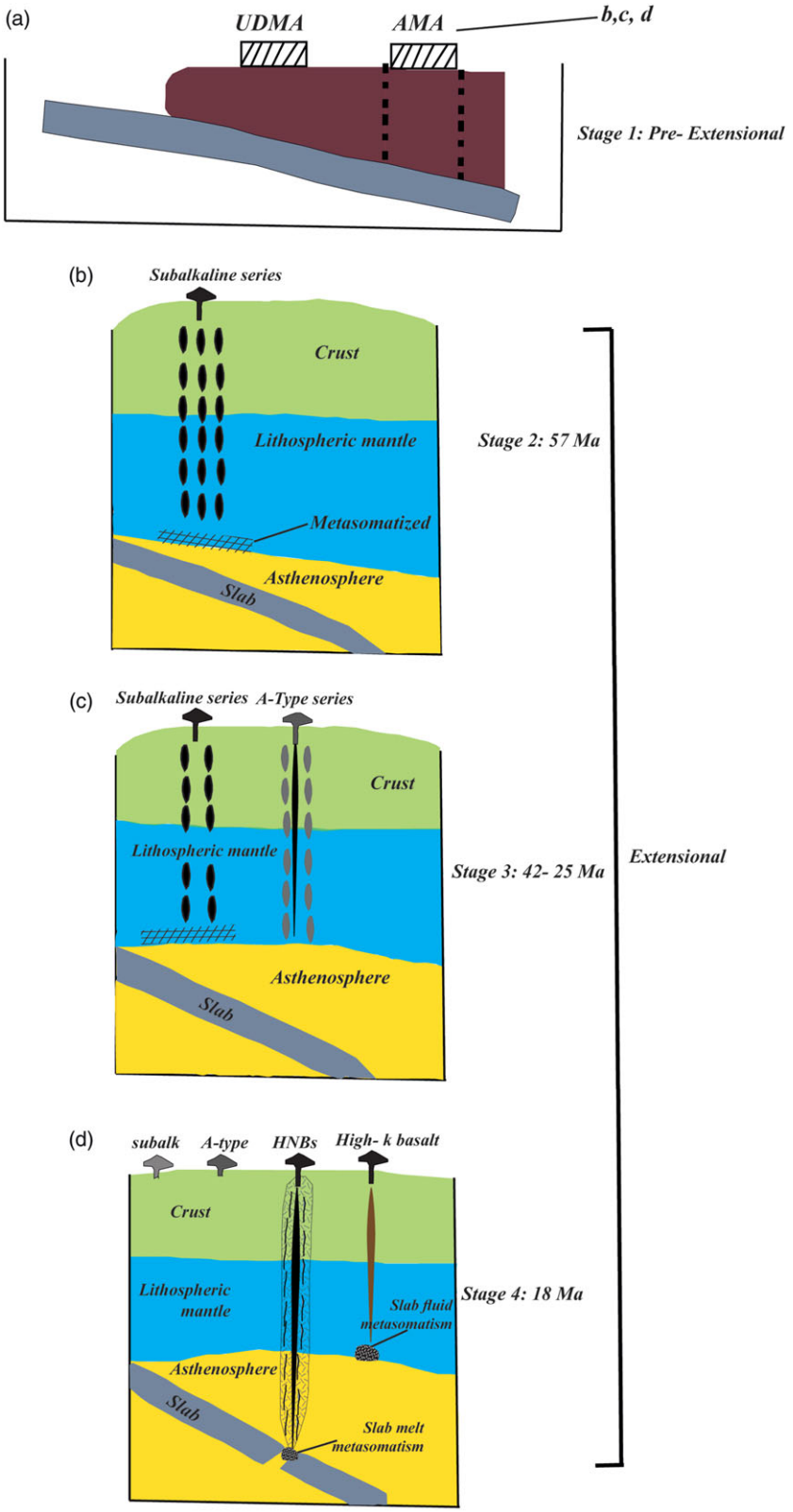

Fig. 15. (Colour online) Geodynamic model summarizing the SE Ahar magmatic compositional evolution through time.

Acknowledgements. This work is derived from the Ph.D. thesis by A.A. Funds and facilities provided by Tarbiat Modares University (TMU) is acknowledged. The authors are grateful for support and friendship provided by colleagues and students from TMU. This manuscript has greatly benefited from thoughtful reviews provided by Prof. I. Neill, Prof. K. Goodenough and an anonymous referee; their reviews are highly appreciated. Handling of the manuscript by Associate Editor, Prof. K. Goodenough is sincerely acknowledged. Whole-rock major- and trace-element analyses were financially supported by the National

Science Foundation of China (41490614). Sr and Nd isotopic analyses were done under the scope of project Geobiotec (UID/GEO/04035/2013), funded by FCT (Portugal). Accommodation during fieldwork was generously provided by the Sungun Mine Complex.

Supplementary material. To view supplementary material for this article, please visit https://doi.org/10.1017/S0016756820000527

References

Agard P, Omrani J, Jolivet L and Mouthereau F (2005) Convergence history across Zagros (Iran): constraints from collisional and earlier deformation. *International Journal of Earth Sciences (Geologische Rundschau)* **94**, 401–19.

Agard P, Omrani J, Jolivet L, Whitechurch H, Vrielynck B, Spakman W, Monie P, Eyer B and Wortel R (2011) Zagros orogeny: a subduction-dominated process. *Geological Magazine* **148**, 692–725. doi: 10.1017/S001675681100046X.

Aghanabati E (2004) *Geology of Iran*. Tehran: Geological Survey and Mineral Exploration Organization of Iran, 586 pp.

Aghazadeh M, Castro A, Badrzadeh Z and Vogt K (2011) Post-collisional polycyclic plutonism from the Zagros hinterland: the Shaivar Dagh plutonic complex, Alborz belt, Iran. *Geological Magazine* **148**, 980–1008.

Aghazadeh M, Castro A, Rashidnejad Omran N, Emami MH, Moinvaziri H and Badrzadeh Z (2010) The gabbro (shoshonitic)-monzonite-granodiorite association of Khankandi pluton, Alborz Mountains, NW Iran. *Journal of Asian Earth Sciences* **38**, 199–219.

Alavi M (1994) Tectonics of the Zagros orogenic belt of Iran: new data and interpretations. *Tectonophysics* **229**, 211–38.

Alavi M (1996) Tectonostratigraphic synthesis and structural style of the Alborz Mountain system in northern Iran. *Journal of Geodynamics* **21**, 1–33.

Aldanmaz E, Pearce JA, Thirwall MF and Mitchell JG (2000) Petrogenetic evolution of late Cenozoic post-collision volcanism in western Anatolia, Turkey. *Journal of Volcanology and Geothermal Research* **102**, 67–95.

Allen MB and Armstrong HA (2008) Arabia–Eurasia collision and the forcing of mid-Cenozoic global cooling. *Palaeogeography, Palaeoclimatology, Palaeoecology* **265**, 52–8.

Allen MB, Ghassemi MR, Shahrabi M and Qorashi M (2003) Accommodation of late Cenozoic shortening in the Alborz range, northern Iran. *Journal of Structural Geology* **25**, 659–72.

Alonso-Perez R, Muntener O and Ulmer P (2009) Igneous garnet and amphibole fractionation in the roots of island arcs: experimental constraints on H_2O undersaturated andesitic liquids. *Contributions to Mineralogy and Petrology* **157**, 541–58.

Anderson JL and Morrison J (2005) Ilmenite, magnetite, and peraluminous Mesoproterozoic anorogenic granites of Laurentia and Baltica. *Lithos* **80**, 45–60.

Asiabanha A and Foden J (2012) Post-collisional transition from an extensional volcanosedimentary basin to a continental arc in the Alborz Ranges, N-Iran. *Lithos* **148**, 98–111.

Atherton MP and Petford N (1993) Generation of sodium-rich magmas from newly underplated basaltic crust. *Nature* **362**, 144–6.

Azizi H and Moinevaziri H (2009) Review of the tectonic setting of Cretaceous to Quaternary volcanism in northwestern Iran. *Journal of Geodynamics* **47**, 167–79.

Babakhani AR, Lesquyer JL and Rico R (1990) *Geological Map of Ahar Quadrangle (Scale 1:250,000)*. Tehran: Geological Survey of Iran.

Babazadeh S, Ghorbani MR, Brocker M, Antonio MD, Cottle J, Gebbing T, Mazzeo FC and Ahmadi P (2017) Late Oligocene–Miocene mantle upwelling and interaction inferred from mantle signatures in gabbroic to granitic rocks from the Urumieh–Dokhtar arc, south Ardestan, Iran. *International Geology Review* **59**, 1590–608.

Ballato P, Uba CE, Landgraf A, Strecker MR, Sudo M, Stockli DF, Friedrich A and Tabatabaei SH (2011) Arabia–Eurasia continental collision: insights from late Tertiary foreland-basin evolution in the Alborz Mountains, northern Iran. *Geological Society of America Bulletin* **123**, 106–31.

Berberian M and King GCP (1981) Towards a paleogeography and tectonic evolution of Iran. *Canadian Journal of Earth Sciences* **18**, 210–65.

Blundy JD, Robinson JAC and Wood BJ (1998) Heavy REE are compatible in clinopyroxene on the spinel lherzolite solidus. *Earth and Planetary Science Letters* **160**, 493–504.

Boztug D and Harlavan Y (2008) K–Ar ages of granitoids unravel the stages of Neo-Tethyan convergence in the Eastern Pontides and Anatolia, Turkey. *International Journal of Earth Sciences (Geologische Rundschau)* **97**, 585–99.

Castillo PR (2008) Origin of the adakite-high-Nb basalt association and its implications for postsubduction magmatism in Baja California, Mexico. *Geological Society of America Bulletin* **120**, 451–62.

Castillo PR, Rigby SJ and Solidum RU (2007) Origin of high field strength element enrichment in volcanic arcs: geochemical evidence from the Sulu Arc, southern Philippines. *Lithos* **97**, 271–88.

Castillo PR, Solidum RU and Punongbayan RS (2002) Origin of high field strength element enrichment in the Sulu Arc, southern Philippines, revisited. *Geology* **30**, 707–10.

Castro M, Aghazadeh M, Badrzadeh Z and Chichorro M (2013) Late Eocene–Oligocene post-collisional monzonitic intrusions from the Alborz magmatic belt, NW Iran. An example of monzonite magma generation from a metasomatized mantle source. *Lithos* **180–181**, 109–27.

Chaharlang R and Ghorbani MR (2020) A hidden crust beneath the central Urumieh-Dokhtar Magmatic Arc revealed by inherited zircon ages, Tafresh, Iran. *Geological Journal*, **55** 3770–81. doi: 10.1002/gj.3631

Chiaradia M (2009) Adakite-like magmas from fractional crystallization and melting assimilation of mafic lower crust (Eocene Macuchi arc, Western Cordillera, Ecuador). *Chemical Geology* **265**, 468–87.

Chiaradia M (2015) Crustal thickness control on Sr/Y signatures of recent arc magmas: an Earth scale perspective. *Scientific Reports* **5**, 8115. doi: 10.1038/srep08115.

Chiu HY, Sun LC, Zarinkoub MH, Mihanadi SS, Khatib MM and Lizuka Y (2013) Zircon U–Pb age constraints from Iran on the magmatic evolution related to Neotethyan subduction and Zagros orogeny. *Lithos* **162–163**, 70–87.

Chung SL, Liu DY, Ji JQ, Chu MF, Lee HY, Wen DJ, Lo CH, Lee TY, Qian Q and Zhang Q (2003) Adakites from continental collision zones: melting of thickened lower crust beneath southern Tibet. *Geology* **31**, 1021–4.

Collins WJ, Beams SD, White AJR and Chappell BW (1982) Nature and origin of A-type granites with particular reference to southeastern Australia. *Contributions to Mineralogy and Petrology* **80**, 189–200.

Dall'Agnol R and Oliveira DC (2007) Oxidized, magnetite-series, rapakivi-type granites of Carajás, Brazil: implications for classification and petrogenesis of A-type granites. *Lithos* **93**, 215–33.

Dargahi S, Arvin M, Pan Y and Babaei A (2010) Petrogenesis of post-collisional A-type granitoids from the Urumieh–Dokhtar magmatic assemblage, Southwestern Kerman, Iran: constraints on the Arabian–Eurasian continental collision. *Lithos* **115**, 190–204.

Davies JH and von Blanckenburg F (1995) Slab breakoff: a model of lithospheric detachment and its test in the magmatism and deformation of collisional orogens. *Earth and Planetary Science Letters* **129**, 85–102.

Defant MJ and Drummond MS (1990) Derivation of some modern arc magmas by melting of young subducted lithosphere. *Nature* **347**, 662–5.

Defant MJ and Drummond MS (1993) Mount St. Helens: potential example of the partial melting of the subducted lithosphere in a volcanic arc. *Geology* **21**, 547–50.

Defant MJ, Jackson TE, Drummond MS, De Boer JZ, Bellon H, Feigenson MD, Maury RC and Stewart RH (1992) The geochemistry of young volcanism throughout western Panama and southern Costa Rica, an overview. *Journal of the Geological Society, London* **149**, 569–79.

Defant MJ, Richerson PM, De Boer JZ, Stewart RH, Maury RC, Bellon H, Drummond MS, Feigenson MD, Maury RC and Jackson TE (1991) Dacite genesis via both slab melting and differentiation: petrogenesis of La Yeguada volcanic complex, Panama. *Journal of Petrology* **32**, 1101–42.

Eby GN (1992) Chemical subdivision of the A-type granitoids: petrogenetic and tectonic implications. *Geology* **20**, 641–4.

Emami MH, Mohamad MIR, Sadeghi M and Omrani SJ (1996) *Magmatic Map of Iran, Scale: 1:1:000:000*. Tehran: Geological Survey of Iran.

Ersoy EY, Palmer MR, Genç SC, Prelević D, Akal C and Uysal I (2017) Chemo-probe into the mantle origin of the NW Anatolia Eocene to Miocene volcanic rocks: implications for the role of, crustal accretion,

subduction, slab roll-back and slab break-off processes in genesis of post-collisional magmatism. *Lithos* **288–289**, 55–71.

Foley SF, Barth MG and Jenner GA (2000) Rutile/melt partition coefficients for trace elements and an assessment of the influence of rutile on the trace element characteristics of subduction zone magmas. *Geochimica et Cosmochimica Acta* **64**, 933–8.

Gao Y, Yang Z, Hou Z, Wei R, Meng X and Tian S (2010) Eocene potassic and ultrapotassic volcanism in south Tibet: new constraints on mantle source characteristics and geodynamic processes. *Lithos* **117**, 20–32.

Ghorbani MR, Graham IT and Ghaderi M (2014) Oligocene–Miocene geodynamic evolution of the central part of Urumieh–Dokhtar Arc of Iran. *International Geology Review*, **56**, 1039–50.

Guest B, Stockli DF, Grove M, Axen GJ and Lam PS (2006) Thermal histories from the central Alborz Mountains, northern Iran: implications for the spatial and temporal distribution of deformation in northern Iran. *Geological Society of America Bulletin* **118**, 1507–21.

Hajian J (2001) *Geology of Tafresh*. Tehran: Geological Survey of Iran, Report No. 82.

Han BF, Wang SG, Jahn BM, Hong DW, Kagami H and Sun YL (1997) Depleted-mantle magma source for the Ulungur River A-type granites from north Xinjiang, China: geochemistry and Nd–Sr isotopic evidence, and implication for Phanerozoic crustal growth. *Chemical Geology* **138**, 135–59.

Hassanzadeh J, Stockli DF, Horton BK, Axen GJ, Stockli LD, Grove M, Schmitt AK and Walker JD (2008) U–Pb zircon geochronology of late Neoproterozoic–Early Cambrian granitoids in Iran: implications for paleogeography, magmatism, and exhumation history of Iranian basement. *Tectonophysics* **451**, 71–96.

Hastie AR, Mitchell SF, Kerr AC, Minifie MJ and Millar IL (2011) Geochemistry of rare high-Nb basalt lavas: are they derived from a mantle wedge metasomatised by slab melts? *Geochimica et Cosmochimica Acta* **75**, 5049–72.

Hidalgo PJ, Vogel TA, Rooney TO, Currier RM and Layer PW (2011) Origin of silicic volcanism in the Panamanian arc: evidence for a two-stage fractionation process at El Valle volcano. *Contributions to Mineralogy and Petrology* **162**, 1115–38.

Horstwood MSA, Kosler J, Gehrels G, Jackson SE, McLean NM, Paton C, Pearson NJ, Sircombe K, Sylvester P, Vermeesch P, Bowring JF, Condon DJ and Schoene B (2016) Community-derived standards for LA-ICP-MS U-(Th-)Pb geochronology – uncertainty propagation, age interpretation and data reporting. *Geostandards and Geoanalytical Research* **40**, 311–32.

Horton BK, Hassanzadeh J, Stockli DF, Axen GJ, Gillis RJ, Guest B, Amini A, Fakhari MD, Zamanzadeh SM and Grove M (2008) Detrital zircon provenance of Neoproterozoic to Cenozoic deposits in Iran: implications for chronostratigraphy and collisional tectonics. *Tectonophysics* **451**, 97–122.

Hou ZQ, Gao YF, Qu XM, Rui ZY and Mo XX (2004) Origin of adakitic intrusives generated during mid-Miocene east–west extension in southern Tibet. *Earth and Planetary Science Letters* **220**, 139–55.

Irvine TN and Baragar WRA (1971) A guide to the chemical classification of the common volcanic rocks. *Canadian Journal of Earth Sciences* **8**, 523–48.

Jackson J, Priestley K, Allen M and Berberian M (2002) Active tectonics of the South Caspian Basin. *Geophysical Journal International* **148**, 214–45.

Jahangiri A (2007) Post-collisional Miocene adakitic volcanism in NW Iran: geochemical and geodynamic implications: *Journal of Asian Earth Sciences* **30**, 433–47. doi: 10.1016/j.jseaes.2006.11.008.

Jahn BM, Wu FY and Chen B (2000a) Massive granitoid generation in Central Asia: Nd isotope evidence and implication for continental growth in the Phanerozoic. *Episodes* **23**, 82–92.

Jahn BM, Wu FY and Chen B (2000b) Granitoids of the Central Asian Orogenic belt and continental growth in the Phanerozoic. *Transactions of the Royal Society of Edinburgh: Earth Sciences* **91**, 181–93.

Jamali H and Mehrabi B (2015) Relationships between arc maturity and Cu–Mo–Au porphyry and related epithermal mineralization at the Cenozoic Arasbaran magmatic belt. *Ore Geology Review* **65**, 487–501.

Kamei A, Miyake Y, Owada M and Kimura JI (2009) A pseudo adakite derived from partial melting of tonalitic to granodioritic crust, Kyushu, southwest Japan arc. *Lithos* **112**, 615–25.

Kamvong T, Zaw K, Meffre S, Mass R, Stein H and Lai CK (2014) Adakites in the Truong Son and Loei fold belts, Thailand and Laos: genesis and implications for geodynamics and metallogeny. *Gondwana Research* **26**, 165–84.

Kaygusuz A, Siebel W, Şen C and Satir M (2008) Petrochemistry and petrology of I-type granitoids in an arc setting: the composite Torul pluton, Eastern Pontides, NE Turkey. *International Journal of Earth Sciences (Geologische Rundschau)* **97**, 739–64.

Keppler H (1996) Constraints from partitioning experiments on the composition of subduction-zone fluids. *Nature* **380**, 237–40.

Le Bas MJ, Le Maitre RW, Streckeisen A and Zanettin B (1986) A chemical classification of volcanic rocks based on the total alkali–silica diagram. *Journal of Petrology* **27**, 445–50.

Lechmann A, Burg JP, Ulmer P, Guillong M and Faridi M (2018) Metasomatized mantle as the source of Mid-Miocene–Quaternary volcanism in NW-Iranian Azerbaijan: geochronological and geochemical evidence. *Lithos* **304–307**, 311–28.

Li SM, Zhu DC, Wang Q, Zhao Z, Zhang LL, Liu SA, Chang QS, Lu YH, Dai JG and Zheng YC (2016) Slab-derived adakites and subslab asthenosphere-derived OIB-type rocks at 156 ± 2 Ma from the north of Gerze, central Tibet: records of the Bangong–Nujiang oceanic ridge subduction during the Late Jurassic. *Lithos* **262**, 456–69.

Liu W (2002) Fluid–rock interaction during subsolidus microtextural development of alkali granite as exemplified by the Saertielieke pluton, Ulungur of the northern Xinjiang, China. *Chemical Geology* **182**, 473–82.

Liu W and Fei PX (2006) Methane-rich fluid inclusions from ophiolitic dunite and post-collisional mafic-ultramafic intrusion: the mantle dynamics underneath the Palaeo-Asian Ocean through to the postcollisional period. *Earth and Planetary Science Letters* **242**, 286–301.

Loiselle MC and Wones DR (1979) Characteristics and origin of anorogenic granites. *Geological Society of America Abstracts with Programs* 11, 468.

Ludwig KR (1991) *ISOPLOT: A Plotting and Regression Program for Radiogenic-Isotope Data, Version 2.53*. U.S. Geological Survey Open-File Report 91–445, 39 pp.

Macpherson CG, Chiang KK, Hall R, Nowell GM, Castillo PR and Thirlwall MF (2010) Plio-Pleistocene intra-plate magmatism from the southern Sulu arc, Semporna peninsula, Sabah, Borneo: implications for high-Nb basalt in subduction zones. *Journal of Volcanology and Geothermal Research* **190**, 25–38

Mahdavi MA and Amini Fazl A (1988) *1:100000 Geologic Map of Ahar, Iran*. Tehran: Geological Survey of Iran.

Marquez A, Oyarzun R, Doblas M and Verma SP (1999) Alkalic (OIB-type) and calcalkalic volcanism in the Mexican volcanic belt: a case of plume-related magmatism and propagating rifting at an active margin? *Geology* **27**, 51–4.

Martin H, Smithies RH, Rapp R, Moyen JF and Charnpion D (2005) An overview of adakite, tonalite-trondhjemite-granodiorite (TTG), and sanukitoid: relationships and some implications for crustal evolution. *Lithos* **79**, 1–24.

Mokhtari MAA, Moinvaziri H, Ghorbani MR and Mehrpartou M (2010) Petrology and petrogenesis of Kamtal intrusion, Eastern Azarbaijan, NW Iran. *Central European Geology* **53**, 79–96.

Moritz R, Rezeau H, Ovtcharova M, Tayan R, Melkonyan R, Hovakimyan S, Ramazanov V, Selby D, Ulianov A, Chiaradia M and Putlitz B (2016) Long-lived, stationary magmatism and pulsed porphyry systems during Tethyan subduction to post-collision evolution in the southernmost Lesser Caucasus, Armenia and Nakhitchevan. *Gondwana Research* **37**, 465–503.

Müller D and Groves DI (1995) *Potassic Igneous Rocks and Associated Gold-Copper Mineralization*. Berlin: Springer-Verlag, 144 pp.

Muntener O, Kelemen PB and Grove TL (2001) The role of H_2O during crystallization of primitive arc magmas under uppermost mantle conditions and genesis of igneous pyroxenites: an experimental study. *Contributions to Mineralogy and Petrology* **141**, 643–58.

Nabatian G, Ghaderi M, Neubauer F, Honarmand M, Lui X, Dong Y, Jiang SY and Bernroider M (2014) Petrogenesis of Tarom high-potassic granitoids in the Alborz–Azarbaijan belt, Iran: geochemical, U–Pb zircon and Sr–Nd–Pb isotopic constraints. *Lithos* **184–187**, 324–45.

Nabavi MH (1976) *An Introduction to Iranian Geology*. Tehran: Special Publication of the Geological Survey of Iran, 110 pp. (in Farsi).

Neill I, Melikestian K, Allen MB, Navasarrdyan G and Kuiper K (2015) Petrogenesis of mafic collision zone magmatism: the Armenian sector of the Turkish–Iranian Plateau. *Chemical Geology* **403**, 24–41.

Okay AI and Sahinturk O (1997) Geology of the Eastern Pontides. In *Regional and Petroleum Geology of the Black Sea and Surrounding Region* (ed. AG Robinson), pp. 292–311. American Association of Petroleum Geologists Memoir 68.

Omrani J, Agard P, Whitechurch H, Benoit M, Prouteau G and Jolivet L (2008) Arc magmatism and subduction history beneath the Zagros Mountains, Iran: a new report of adakites and geodynamic consequences. *Lithos* **106**, 380–98.

Paton C, Hellstrom J, Paul B, Woodhead J and Hergt J (2011) Freeware for the visualisation and processing of mass spectrometric data. *Journal of Analytical Atomic Spectrometry* **26**, 2508.

Pearce JA, Harris NBW and Tindle AG (1984) Trace element discrimination diagrams for the tectonic interpretation of granitic rocks. *Journal of Petrology* **25**, 956–83.

Pearce JA, Thirlwall MF, Ingram G, Murton BJ, Arculus RJ and van der Laan SR (1992) Isotopic evidence for the origin of boninites and related rocks drilled in the Izu-Bonin (Ogasawara) forearc, Leg 1251. In *Proceedings of the Ocean Drilling Program, Scientific Results, vol. 125* (eds P Fryer, JA Pearce, LB Stokking, JR Ali, R Arculus, D Ballotti, MM Burke, G Ciampo, JA Haggerty, RB Haston, D Heling, MA Hobart, T Ishii, LE Johnson, Y Lagabrielle, FW McCoy, H Maekawa, MS Marlow, G Milner, MJ Motti, BJ Murton, SP Phipps, CA Rigsby, KL Saboda, B Stabell, S van der Laan and Y Xu), pp. 237–61. College Station, Texas.

Peccerillo A and Taylor SA (1976) Geochemistry of Eocene calc-alkaline volcanic rocks from the Kastamonu area, Northern Turkey. *Contributions to Mineralogy and Petrology* **58**, 63–81.

Petford N and Atherton M (1996) Na-rich partial meltings from newly underplated basaltic crust: the Cordillera Blanca Batholith, Peru. *Journal of Petrology* **37**, 1491–521.

Pickering-Witter J and Johnston AD (2000) The effects of variable bulk composition on the melting systematics of fertile peridotitic assemblage. *Contributions to Mineralogy and Petrology* **140**, 190–211.

Plank T (2005) Constraints from thorium/lanthanum on sediment recycling at subduction zones and the evolution of the continents. *Journal of Petrology* **46**, 921–44.

Polat A and Hofmann A (2003) Alteration and geochemical patterns in the 3.7–3.8 Ga Isua greenstone belt, West Greenland. *Precambrian Research* **126**, 197–218.

Prouteau G, Scaillet B, Picavant M, Maury R (2001) Evidence for mantle metasomatism by hydrous silicic melts derived from subducted oceanic crust. *Nature* **410**, 197–200.

Rahmati-Ilkhchi M, Faryad SW, Holub FV, Kosler J and Frank W (2011) Magmatic and metamorphic evolution of the Shotur Kuh metamorphic complex (Central Iran). *International Journal of Earth Sciences (Geologische Rundschau)* **100**, 45–62.

Ramezani J and Tucker RD (2003) The Saghand region, Central Iran: U–Pb geochronology, petrogenesis and implications for Gondwana tectonics. *American Journal of Science* **303**, 622–65.

Rapp RP and Watson EB (1995) Dehydration melting of metabasalt at 8–32 kbar: implications for continental growth and crust–mantle recycling. *Journal of Petrology* **36**, 891.

Reagan MK and Gill JB (1989) Coexisting calcalkaline and high-niobium basalts from Turrialba volcano, Costa Rica: implications for residual titanites in arc magma sources. *Journal of Geophysical Research* **94**, 4619–33.

Rezeau H, Moritz R, Leothold J, Hovakimyan S, Tayan R and Chiaradia M (2017) 30 Myr of Cenozoic magmatism along the Tethyan margin during Arabia–Eurasia accretionary orogenesis (Meghri–Ordubad pluton southernmost Lesser Caucasus). *Lithos* **288–289**, 108–24.

Rolland Y (2017) Caucasus collisional history: review of data from East Anatolia to West Iran. *Gondwana Research* **49**, 130–46.

Saccani E (2015) A new method of discriminating different types of post-Archean ophiolitic basalts and their tectonic significance using Th–Nb and Ce–Dy–Yb systematics. *Geoscience Frontiers* **6**, 481–501.

Sajona FG, Maury RC, Bellon H, Cotton J and Defant M (1996) High field strength element enrichment of Pliocene-Pleistocene island arc basalts, Zamboanga Peninsula, western Mindanao (Philippines). *Journal of Petrology* **37**, 693–726.

Sajona FG, Maury RC, Bellon H, Cotton J, Defant MJ, Pubellier M and Rangin C (1993) Initiation of subduction and the generation of slab melts in western and eastern Mindanao, Philippines. *Geology* **21**, 1007–10.

Shaw JE, Baker JA, Menzies MA, Thirlwall MF and Ibrahim KM (2003) Petrogenesis of the largest intraplate volcanic field on the Arabian plate (Jordan): a mixed lithosphere-asthenosphere source activated by lithospheric extension. *Journal of Petrology* **44**, 1657–79.

Stampfli GM, Hochard C, Verard C, Wilhem C and vonRaumer J (2013) The formation of Pangea. *Tectonophysics* **593**, 1–19.

Stöcklin J (1968) Structural history and tectonics of Iran: a review. *American Association of Petroleum Geologists Bulletin* **52**, 1229–58.

Sun SS and McDonough WF (1989) Chemical and isotopic systematics of oceanic basalts: implications for mantle composition and processes. In *Magmatism in the Ocean Basins* (eds AD Saunders and MJ Norry), pp. 313–45. Geological Society of London, Special Publication no. 42.

Thirlwall MF, Smith TE, Graham AM, Theodorou N, Hollings P, Davidson JP and Arculus RJ (1994) High field strength element anomalies in arc lavas; source or process? *Journal of Petrology* **35**, 819–38.

Turner SP, Foden JD and Morrison RS (1992) Derivation of some A-type magmas by fractionation of basaltic magma; an example from the Padthaway Ridge, South Australia. *Lithos* **28**, 151–79.

van Huen J and Allen M (2011) Continental collision and slab break-off: a comparison of 3-D numerical models with observations. *Earth and Planetary Science Letters* **302**, 27–37.

Verdel C, Wernicke BP, Hassanzadeh J and Guest B (2011) A Paleogene extensional arc flare-up in Iran. *Tectonics* **30**, TC3008. doi: 10.1029/2010TC002809.

Verma SP and Nelson SA (1989) Isotopic and trace element constraints on the origin and evolution of alkaline and calcalkaline magmas in the northwestern Mexican volcanic belt. *Journal of Geophysical Research* **94**, 4531–44.

Vincent SJ, Allen MB, Ismail-Zadeh AD, Flecker R, Foland KA and Simmons MD (2005) Insights from the Talysh of Azerbaijan into the Paleogene evolution of the South Caspian region. *Geological Society of America Bulletin* **117**, 1513–33.

von Raumer JF, Stampfli GM, Arenas R and Sánchez Martínez S (2015) Ediacaran to Cambrian oceanic rocks of the Gondwana margin and their tectonic interpretation. *International Journal of Earth Sciences (Geologische Rundschau)* **104**, 1107–21.

Wang W, Pandit MK, Zhao JH, Chen WT and Zheng JP (2018) Slab break-off triggered lithosphere-asthenosphere interaction at a convergent margin: the Neoproterozoic bimodal magmatism in NW India. *Lithos* **296**, 281–96.

Wang C, Song S, Niu Y, Allen MB, Su L, Wei C, Zhang G and Fu B (2017) Long-lived melting of ancient lower crust of the North China Craton in response to Paleo-Pacific plate subduction, recorded by adakitic rhyolite. *Lithos* **292–293**, 437–51.

Wang Q, Xu JF, Jian P, Bao ZW, Zhao ZH, Li CF, Xiong XL and Ma JL (2006) Petrogenesis of adakitic porphyries in an extensional tectonic setting, Dexing, South China: implications for the genesis of porphyry copper mineralization. *Journal of Petrology* **47**, 119–44.

Whalen JB, Currie KL and Chappell BW (1987) A-type granites: geochemical characteristics, discrimination and petrogenesis. *Contributions to Mineralogy and Petrology* **95**, 407–19.

Wiedenbeck M, Alle P, Corfu F, Griffin Wl, Meier M and Oberli F (1995) Three natural zircon standards for U–Th–Pb, Lu–Hf, trace element and REE analyses. *Geostandards Newsletter* **19**, 1–23.

Wu F, Jahn B, Wilde S and Sun D (2000) Phanerozoic crustal growth: U–Pb and Sr–Nd isotopic evidence from the granites in northeastern China. *Tectonophysics* **328**, 89–113.

Wu FY, Sun DY, Li HM, Jahn BM and Wilde S (2002) A-type granites in northeastern China: age and geochemical constraints on their petrogenesis. *Chemical Geology* **187**, 143–73.

Xie Q, Zhang Z, Campos E, Cheng Z, Fei X, Liu B, Qiu Y, Santosh M, Ke S and Xu L (2018) Magnesium isotopic composition of continental arc

andesites and the implications: a case study from the El Laco volcanic complex, Chile. *Lithos* **318–319**, 91–103.

Yang W, Niu H, Shan Q, Luo Y, Sun W, Li C, Li N and Yu X (2012) Late Paleozoic calcalkaline to shoshonitic magmatism and its geodynamic implications, Yuximolegai area, western Tianshan, Xinjiang. *Gondwana Research* **22**, 325–40.

Yeganehfar H, Ghorbani MR, Shinjo R and Ghaderi M (2013) Magmatic and geodynamic evolution of Urumieh– Dokhtar basic volcanism, Central Iran: major, trace element, isotopic, and geochronologic implications. *International Geology Review* **55**, 767–86.

Yogodzinski GM, Kay RW, Volynets ON, Koloskov AV And Kay SM (1995) Magnesian andesite in the western Aleutian Komandorsky region: implications for slab melting and processes in the mantle wedge. *Geological Society of America Bulletin* **107**, 505–19.

Yuan L, Zhang X, Xue F, Lu Y and Zong K (2016) Late Permian high-Mg andesite and basalt association from northern Liaoning, North China: insights into the final closure of the Paleo-Asian ocean and the orogen–craton boundary. *Lithos* **258–259**, 58–76.

Zhang H, Niu H, Sato H, Yu X, Shan Q, Zhang B, Ito J and Nagao T (2005) Late Palaeozoic adakites and Nb-enriched basalts from northern Xinjiang northwest China: evidence for the southward subduction of the Paleo-Asian Oceanic plate. *Island Arc* **14**, 55–68.

Zhao ZH, Wang ZG, Zou TR and Masuda A (1996) Study on petrogenesis of alkali-rich intrusive rocks of Ulungur, Xinjiang. *Geochimica* **25**, 205–20 (in Chinese with English abstract).

Zindler A and Hart SR (1986) Chemical geodynamics. *Annual Review of Earth and Planetary Sciences* **14**, 493–571.